Coupling effect of wall slip and spanwise oscillation on drag reduction in turbulent channel flow

Zexiang Li [1] Songsong Ji,[1] Huiling Duan,[1,2] Shilong Lan,[3] Jinbai Zhang [3] and Pengyu Lv [1,*]

[1]*State Key Laboratory for Turbulence and Complex Systems, Department of Mechanics and Engineering Science, BIC-ESAT, College of Engineering, Peking University, Beijing 100871, China*
[2]*Key Laboratory of High Energy Density Physics Simulation, Center for Applied Physics and Technology, Peking University, Beijing 100871, China*
[3]*National Laboratory of Computational Fluid Dynamics, Beihang University, Beijing 100191, China*

The coupling effect of the isotropic wall slip and the spanwise oscillation boundary conditions on the drag reduction and turbulence properties are studied by direct numerical simulations. As the slip length increases, the drag reduction gradually changes from the oscillation dominated to the slip dominated. The increase of slip length will decrease the maximum spanwise velocity of the fluid on the wall, which is responsible for the decreased ability of the oscillatory wall motion to reduce the skin-friction drag. The drag reduction decomposition shows that the contribution from the modifications of turbulent dynamics will undergo a shift from drag increase to drag reduction as the isotropic slip length increases. Compared with the respective no-slip reference flow, the drag reduction of wall slip in laminar and turbulent channel flows can be expressed in a unified form versus the outer scale slip length. Furthermore, many aspects of the turbulence properties are influenced by the coupling effect. First, the wall slip condenses the envelope range of the phase fluctuations caused by the oscillatory wall motion, as well as the magnitude of the periodic fluctuation of the phase-averaged friction coefficient. Second, an unexpected property of the coupled boundary condition is found that the existence of the Stoke layer delays the relaminarization process caused by the large slip length. Third, the wall slip would narrow the periodic inclination of the streaks and then inhibit the energy transfer process in the horizontal direction. Fourth, in terms of phase, the Stokes strain and the shear angle have the same lag phase with the spanwise velocity, while the hysteresis of turbulent dynamics leads to the larger lag phase of the streaks and phase-averaged friction coefficient. These new features are valuable for increasing knowledge on this topic.

I. INTRODUCTION

Turbulent drag reduction is an important way to improve the endurance and reduce the energy consumption of marine vessels and underwater vehicles, which is of great significance to sustainable development. The physical basis of turbulent drag reduction can be summarized as the influences of boundary conditions on the coherent structures and the bursting processes [1]. Many flow control schemes are therefore proposed to reduce the skin-friction drag [1,2], including passive (e.g., superhydrophobic surfaces) and active (e.g., spanwise oscillation) strategies. Numerical simulation
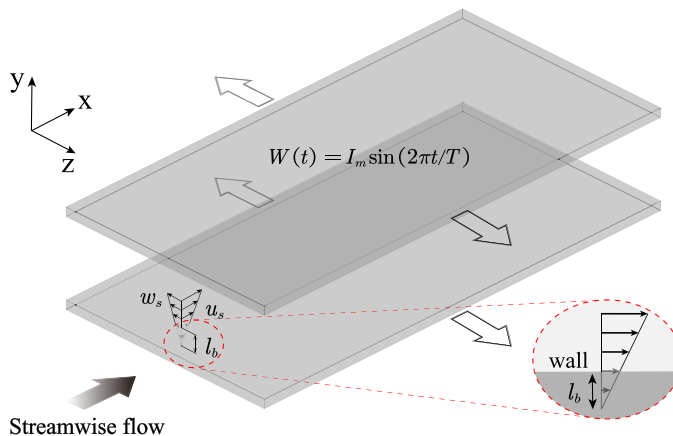
---

*lvpy@pku.edu.cn

FIG. 1. Schematic diagram of the physical problem. The coupled boundary condition of wall slip and spanwise oscillation. $W(t)$ is the oscillating wall velocity in the spanwise direction. u_s and w_s is the streamwise and spanwise slip velocities of the fluid on the wall, respectively. l_b is the isotropic slip length.

method plays an important role in the study of turbulent drag reduction, and direct numerical simulations (DNS) is favored by researchers for its accurate identification of the flow field.

As a passive drag reduction strategy, superhydrophobic surfaces [3–7], inspired by the water-repellent properties of many surfaces in nature [4], can be used for drag reduction in both laminar [8–15] and turbulent [15–34] flow regimes. Experimental studies [18–21] have shown that the effects of superhydrophobic surfaces on the flows can be equivalent to the slip boundary condition, in which the slip length is a key parameter to evaluate the performance of the slippage. The slip length l_b is the ratio of the finite slip velocity on the wall to the local wall-normal derivative of the velocity [4,11,16,23,25], as illustrated in the inset of Fig. 1. The boundary condition on a superhydrophobic surface with randomly distributed textures can be represented by an isotropic slip length in both streamwise and spanwise directions [31]. The effect of slip length on the drag reduction of wall turbulence was first investigated by Min *et al.* [23], showing that in order to have a noticeable drag reduction, the slip length must be greater than a critical value. Fukagata *et al.* [16] deduced a theoretical framework of drag reduction based on the law of the wall, which is in good agreement with the DNS results within the whole range of slip length (hereafter, referred to as the FKK theory). Busse *et al.* [25] proposed a modification on the FKK theory, which improves the prediction for the change of drag for small slip length. Aghdam *et al.* [15] further extended the FKK theory to the situation where the slip length is shear dependent. According to the literature, the drag reduction achieved by isotropic slip is almost independent of the Reynolds number [16,25,34]. The drag reduction mechanism is generally explained by the influence of the slip boundary condition on the turbulent dynamics. In the numerical study of Busse *et al.* [25], the results showed that the slip boundary condition would affect the intermittency degree of the probability density function of the wall shear stress, and a high streamwise slip helps to make the streaks more regular. Based on the mechanism analysis, Rastegari *et al.* [26,33] proposed a general expression of the magnitude of drag reduction, i.e., DR $= u_s/U_b + O(\varepsilon)$, in which, u_s is the mean slip velocity on the wall and U_b is the bulk mean velocity. u_s/U_b comes from the effective slip on the wall and $O(\varepsilon)$ results from the modifications to the turbulent dynamics, where $O(\varepsilon)$ contributes to no more than 20% of the total drag reduction. In these previous investigations, the wall itself is stationary. It is still unclear how the effective slip affects the drag reduction as well as the turbulent dynamics under a boundary condition of wall motion.

In fact, active boundary motion can also achieve drag reduction, in which the spanwise oscillation is a typical method. As an active drag reduction strategy, spanwise wall oscillation [35–45] has

been widely investigated on the condition that the wall is no-slip. For the first time, Jung *et al.* [38] applied the spanwise wall oscillation to the turbulent channel flow and studied a wide range of nondimensional oscillation periods T^+. Under the optimal oscillation period ($T^+ \approx 100$), the drag reduction can be up to 40%. Quadrio *et al.* [42] produced a drag reduction database of various oscillation periods and amplitudes by DNS, based on which a scaling parameter was addressed to describe the amount of drag reduction. The parameter was linearly related to the drag reduction on condition that the oscillation period was less than twice the typical lifetime of the near-wall structures. To reveal the mechanism of drag reduction by spanwise oscillation, Choi [39] carried out an experimental investigation on the near-wall structures modified by the oscillatory wall motion and argued that the drag reduction is the result of the weakened stretching of the quasi-streamwise vortices induced by the negative spanwise vorticity. Through the discussion on turbulence statistics, Touber *et al.* [43] concluded that the unsteady cross-flow straining inhibits the contribution of turbulence to the wall shear stress, leading to the drag reduction. For the parameters of spanwise oscillation, there is an optimal oscillation period for drag reduction, and the reduction is positively correlated with the velocity amplitude.

In summary, the drag reduction mechanism of spanwise oscillation is quite different from that of wall slip. The former can modulate turbulence statistics and coherent structures periodically [40,43], while the latter has a limited effect on the turbulent dynamics [26,33]. In the current work, the wall slip is applied to the oscillatory turbulent channel flow to explore the drag reduction performance. The influence of this coupled boundary condition (wall slip and spanwise oscillation) on the turbulence properties are also investigated. The motivation and the main implication of this study lie in the quantitative understanding of the drag reduction and the turbulent dynamics under the coupling effect of wall slip and spanwise oscillation, which is helpful to extend the cognition of wall turbulence evolution under coupled boundary conditions.

The paper is organized as follows. In Sec. II, the numerical methodology is introduced. In Sec. III, the drag reduction results are shown in Sec. III A, the coupling phenomenon is illustrated in Sec. III B, and the drag reduction decomposition is conducted in Sec. III C. In Sec. IV, the influences of the coupling effect on turbulence properties are discussed from four perspectives: the turbulence statistics, the quadrant analysis, the phase-averaged properties, and the coherent structures. They are illustrated in Secs. IV A, IV B, IV C, and IV D, respectively. Finally, in Sec. V, the conclusions are presented.

II. METHODOLOGY

The schematic diagram of the physical problem studied in the current work is shown in Fig. 1, which presents a channel flow. The isotropic slip boundary condition is coupled with the spanwise oscillatory wall motion. The physical model of isotropic slip is a superhydrophobic surface with randomly distributed textures [31]. The ideal assumption is adopted, i.e., the slip boundary is always maintained as flat.

The channel flow is governed by the incompressible Navier-Stokes equations, which can be expressed as the Lamb form:

$$\nabla \cdot \boldsymbol{u} = 0, \tag{1}$$

$$\frac{\partial \boldsymbol{u}}{\partial t} = \boldsymbol{u} \times \boldsymbol{\omega} - (\nabla \Pi + \boldsymbol{f}) + \nu \nabla^2 \boldsymbol{u}, \tag{2}$$

where $\boldsymbol{u}$ is the velocity vector (the velocity components in the streamwise, spanwise, and wall-normal directions are u, w, and v, respectively), $\boldsymbol{\omega} = \nabla \times \boldsymbol{u}$ is the vorticity vector, $\Pi = p/\rho + |\boldsymbol{u} \cdot \boldsymbol{u}|/2$ is the total pressure, p is the pressure fluctuation, ρ is the fluid density, $\boldsymbol{f}$ is the mean streamwise pressure gradient, and ν is the kinematic viscosity of the fluid. The channel flow is driven by $\boldsymbol{f}$, which is adjusted in each time step to maintain a constant flow rate. The Fourier-Chebyshev pseudospectral method is employed to solve the equations. Fourier expansions are used

TABLE I. The grid parameters of the simulations.

Re_b	$\mathrm{Re}_{\tau 0}$	$L_x \times L_y \times L_z$	$N_x \times N_y \times N_z$	Δx^{+0}	Δy^{+0}	Δz^{+0}
2800	180	$4\pi h \times 2h \times 2\pi h$	$256 \times 128 \times 256$	8.8	0.05-4.4	4.4
7000	396	$2\pi h \times 2h \times \pi h$	$256 \times 256 \times 256$	9.7	0.03-4.9	4.9

for spatial discretization of the governing equations in both streamwise and spanwise directions, while Chebyshev polynomials are used in the wall-normal direction. A second-order time-splitting method [46] is adopted for time advancement.

In the current work, two bulk Reynolds numbers Re_b are considered, 2800 and 7000. $\mathrm{Re}_b = U_b h / \nu$, where U_b is the bulk mean velocity, and h is the half channel height. For the turbulent baseline flow, i.e., the flow without wall slip and spanwise oscillation, the corresponding friction Reynolds numbers $\mathrm{Re}_{\tau 0}$ are 180 and 396, respectively. $\mathrm{Re}_{\tau 0} = u_{\tau 0} h / \nu$, where $u_{\tau 0}$ is friction velocity of the turbulent baseline flow. For the cases of $\mathrm{Re}_{\tau 0} = 180$, the size of the computing domain is $4\pi h \times 2h \times 2\pi h$ in the streamwise, wall-normal, and spanwise directions, respectively. For the cases at higher Reynolds number $\mathrm{Re}_{\tau 0} = 396$, a reduced domain size $2\pi h \times 2h \times \pi h$ is used to save the computational cost. Here, although the domain size for the higher Reynolds number is reduced, it is sufficient to capture the mean streamwise pressure gradient and the change in drag, which has been validated by Busse *et al.* [25]. The grid parameters are listed in Table I. The grids in the normal direction are nonuniform. For the cases of $\mathrm{Re}_{\tau 0} = 180$, the minimum spacing near the wall is $\Delta y^{+0} \approx 0.05$, and the maximum spacing at the center of the channel is $\Delta y^{+0} \approx 4.4$. The domain size ($L_x, L_y, L_z$), grid size ($N_x, N_y, N_z$), and nondimensional grid resolution ($\Delta x^{+0}, \Delta y^{+0}, \Delta z^{+0}$) for both cases of $\mathrm{Re}_{\tau 0} = 180$ and $\mathrm{Re}_{\tau 0} = 396$ are comparable to those of the related studies [16,25]. Hereafter, the superscripts $+0$ and $+$ denote the normalization using the wall units of the turbulent baseline flow and the actual flow, respectively.

The upper and lower walls of the channel sinusoidally oscillate in the spanwise direction, with the wall velocity $W(t) = I_m \sin(2\pi t / T)$, where I_m is the wall-velocity amplitude and T is the oscillation period. The dimensionless forms of the wall-velocity amplitude and the oscillation period are $I_m^{+0} = I_m / u_{\tau 0}$ and $T^{+0} = T u_{\tau 0}^2 / \nu$, respectively. The optimal oscillation period of the turbulent channel flow at low Reynolds number is $T^{+0} \approx 100$ [45]. A number of I_m^{+0} and T^{+0} are considered in the current work. The isotropic slip is given by the Navier slip boundary condition, $u_s = l_b \partial u / \partial y |_{\mathrm{wall}}$ and $w_s = l_b \partial w / \partial y |_{\mathrm{wall}}$, where l_b is the isotropic slip length. The dimensionless forms of the slip length based on the outer and inner length scales are $l_b^* = l_b / h$ and $l_b^{+0} = l_b / \delta_\nu$, respectively, where $\delta_\nu \equiv \nu / u_{\tau 0}$ is the viscous length scale of the turbulent baseline flow. The coupled boundary condition is given by specifying the oscillating wall velocity $W(t)$ and the slip length l_b. The actual velocity components of the fluid on the wall are

$$u|_{\pm h} = l_b \left.\frac{\partial u}{\partial n}\right|_{\pm h}, \quad v|_{\pm h} = 0, \quad w|_{\pm h} = I_m \sin\frac{2\pi}{T} t + l_b \left.\frac{\partial w}{\partial n}\right|_{\pm h}, \tag{3}$$

where n is the inward pointing unit normal vector and $y = \pm h$ represent the upper and lower walls of the channel.

The simulation parameters of all the cases in the current work are listed in Table II. The coupled boundary condition involves three parameters as illustrated in Eq. (3): slip length, oscillation amplitude, and oscillation period. In order to save the computational cost, the simulation parameters are selected as follows. For the cases of $\mathrm{Re}_{\tau 0} = 180$, 22 combinations of oscillation amplitude and period are considered. Apart from the combination of $I_m^{+0} = 0$ and $T^{+0} = 0$, the rule for the combination of oscillation amplitude and period follows that I_m^{+0} ranges from 2 to 20 at fixed $T^{+0} = 92$ and T^{+0} ranges from 23 to 276 at fixed $I_m^{+0} = 12$. The slip length l_b^{+0} changes from 0 to 100 or from 0 to 180 for each combination. For the cases of $\mathrm{Re}_{\tau 0} = 396$, only two combinations of oscillation amplitude and period are considered ($I_m^{+0} = 0$, $T^{+0} = 0$ and $I_m^{+0} = 12$, $T^{+0} = 92$), and

TABLE II. The simulation parameters. The turbulent baseline flow corresponds to the combination of $I_m^{+0} = 0$, $T^{+0} = 0$, and $l_b^{+0} = 0$.

$\mathrm{Re}_{\tau 0}$	I_m^{+0}	T^{+0}	l_b^{+0}
180	0	0	0, 0.1, 0.32, 1, 3.2, 7, 10, 15, 21, 32, 50, 72, 100, 135, 180
180	2	92	0, 0.1, 0.32, 1, 3.2, 10, 32, 100
180	4	92	0, 0.1, 0.32, 1, 3.2, 10, 32, 100
180	6	92	0, 0.1, 0.32, 1, 3.2, 10, 32, 100
180	8	92	0, 0.1, 0.32, 1, 3.2, 10, 32, 100
180	10	92	0, 0.1, 0.32, 1, 3.2, 10, 32, 100
180	12	92	0, 0.1, 0.32, 1, 3.2, 7, 10, 15, 21, 32, 50, 72, 100, 135, 180
180	14	92	0, 0.1, 0.32, 1, 3.2, 10, 32, 100
180	16	92	0, 0.1, 0.32, 1, 3.2, 10, 32, 100
180	18	92	0, 0.1, 0.32, 1, 3.2, 10, 32, 100
180	20	92	0, 0.1, 0.32, 1, 3.2, 10, 32, 100
180	12	23	0, 0.1, 0.32, 1, 3.2, 10, 32, 100
180	12	46	0, 0.1, 0.32, 1, 3.2, 10, 32, 100
180	12	69	0, 0.1, 0.32, 1, 3.2, 10, 32, 100
180	12	115	0, 0.1, 0.32, 1, 3.2, 10, 32, 100
180	12	138	0, 0.1, 0.32, 1, 3.2, 10, 32, 100
180	12	161	0, 0.1, 0.32, 1, 3.2, 10, 32, 100
180	12	184	0, 0.1, 0.32, 1, 3.2, 7, 10, 15, 21, 32, 50, 72, 100, 135, 180
180	12	207	0, 0.1, 0.32, 1, 3.2, 10, 32, 100
180	12	230	0, 0.1, 0.32, 1, 3.2, 10, 32, 100
180	12	253	0, 0.1, 0.32, 1, 3.2, 10, 32, 100
180	12	276	0, 0.1, 0.32, 1, 3.2, 10, 32, 100
396	0	0	0, 0.1, 0.32, 1, 3.2, 7, 10, 15, 21, 32, 50, 72, 100, 135, 180
396	12	92	0, 0.1, 0.32, 1, 3.2, 7, 10, 15, 21, 32, 50, 72, 100, 135, 180

l_b^{+0} changes from 0 to 180 for each combination. The total number of cases for the two Reynolds numbers is 227.

For all of the cases in the current work, after approaching statistically stationary, each case is calculated long enough to obtain the concerned turbulence statistics, especially the skin-friction drag. In case of simulations with spanwise oscillation, the phase average is also conducted. For all the cases, including the turbulent baseline flow and the slip flow without oscillation, the ensemble average results are averaged in $320h/U_b$ and $82h/U_b$ nondimensional time for the cases of $\mathrm{Re}_{\tau 0} = 180$ and $\mathrm{Re}_{\tau 0} = 396$, respectively. With the exception of a few cases in which the T^{+0} is greater than 184, these two time lengths are set to contain at least 20 oscillation periods. Taking the cases of $\mathrm{Re}_{\tau 0} = 180$ with $T^{+0} = 184$ for example, $320h/U_b$ contains around 20 oscillation periods. For the cases of $\mathrm{Re}_{\tau 0} = 396$ with $T^{+0} = 92$, $82h/U_b$ also contains around 20 oscillation periods.

Like Agostini *et al.* [45], the decomposition of a physical quantity X in the oscillatory turbulent flow can be written as

$$X = \tilde{X} + X' = \langle X \rangle + \hat{X} + X', \tag{4}$$

where $\tilde{X}$ is the phase-averaged value (i.e., the wall-averaged result under the same phase), X' is the stochastic fluctuation, $\tilde{X} = \langle X \rangle + \hat{X}$, $\langle X \rangle$ is the time-averaged value (i.e., the wall-averaged result under all phases), and $\hat{X}$ is the periodic fluctuation. $\tilde{X}$ is calculated from

$$\tilde{X}|_\phi = \frac{1}{N} \sum_{n=1}^{N} \left[\frac{1}{N_x N_z} \sum_{i,k=1,1}^{N_x, N_z} X_{i,k}|_{\phi+(n-1)T} \right], \tag{5}$$
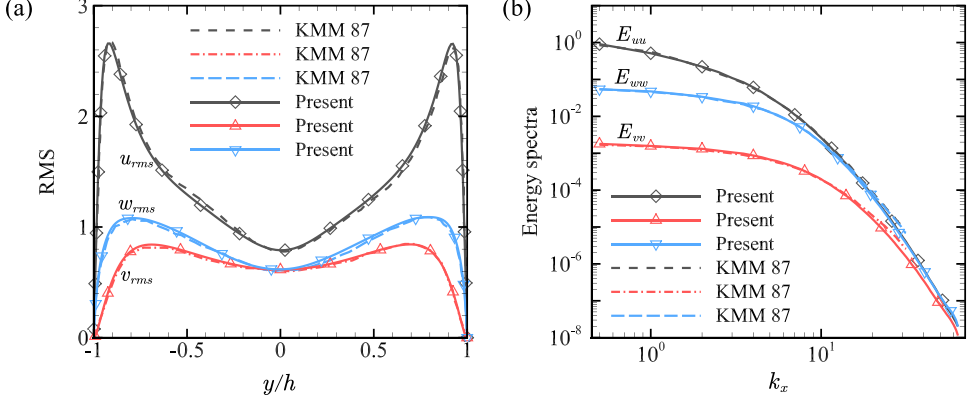
FIG. 2. Validation of the numerical method. (a) The RMS velocity fluctuations scaled with $u_{\tau 0}$ in global coordinates. (b) Streamwise one-dimensional energy spectra of $y^{+0} = 5.4$ (scaled with $u_{\tau 0}^2/2$) versus the streamwise wave number k_x. "Present" represents the result of the current work. "KMM 87" represents the result of Kim *et al.* [47]. Case $\text{Re}_{\tau 0} = 180$.

where $\phi \in \{0, T\}$, i, k are x, z grid indices, and N is the number of periods over which averaging is performed.

For the turbulent baseline flow of the $\text{Re}_{\tau 0} = 180$ cases, the root-mean-square (RMS) velocity fluctuations and the streamwise one-dimensional energy spectra of $y^{+0} = 5.4$ are shown in Fig. 2 to illustrate the accuracy of the algorithm and the adequacy of the grid resolutions, respectively. The RMS velocity fluctuations are in good agreement with the results of Kim *et al.* [47] throughout the channel, as shown in Fig. 2(a). In Fig. 2(b), it can be confirmed that the mesh is adequate. The energy density of the high wave numbers is several orders of magnitude lower than that of the low wave numbers, and there is no energy pile-up at high wave numbers, indicating that the energy transferred from the energy-containing scales to the dissipation scales can be dissipated without accumulation.

III. COUPLING EFFECT ON DRAG REDUCTION

In this section, the drag reduction analysis will be conducted. First, the drag reduction results are shown in Sec. III A. Then, in Sec. III B, the coupling phenomenon is illustrated, which can be used to explain the variation of drag reduction under the coupled boundary condition. Finally, in Sec. III C, the drag reduction is quantitatively decomposed through the outer scale slip length.

A. Drag reduction results

The drag reduction is defined as:

$$\text{DR} = \frac{(\langle C_f \rangle_{\text{base}} - \langle C_f \rangle)}{\langle C_f \rangle_{\text{base}}}, \tag{6}$$

where $\langle C_f \rangle_{\text{base}}$ is the (time-averaged) mean friction coefficient of the turbulent baseline flow and $\langle C_f \rangle$ is the mean friction coefficient of the real flow. Specify DR_{osci}, DR_{slip}, and DR_{coup} as the drag reductions under three different boundary conditions, i.e., the spanwise oscillation boundary condition (no-slip wall), the Navier slip boundary condition (stationary wall), and the coupled boundary condition, respectively. The drag reduction loss DR_{loss} is defined as Eq. (7) to indicate the coupling effect on the drag reduction,

$$\text{DR}_{\text{loss}} = \text{DR}_{\text{osci}} + \text{DR}_{\text{slip}} - \text{DR}_{\text{coup}}. \tag{7}$$

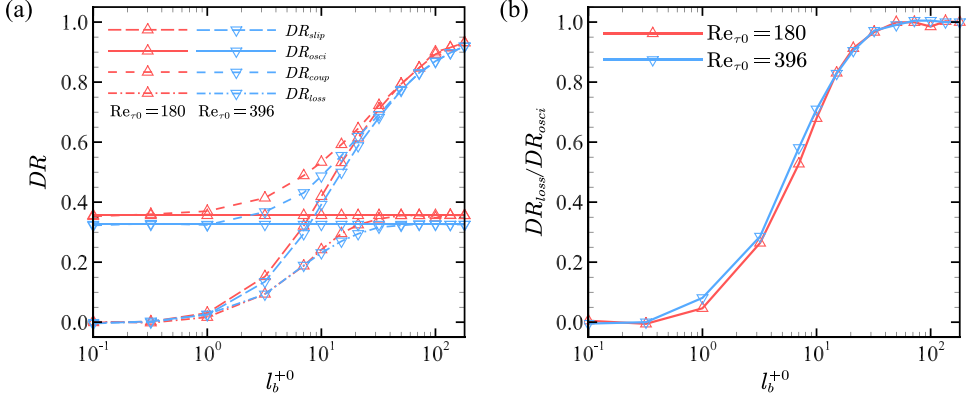FIG. 3. (a) DR and (b) DR_{loss}/DR_{osci} versus the slip length l_b^{+0}. The oscillation parameters corresponding to DR_{osci} and DR_{coup} are $I_m^{+0} = 12$ and $T^{+0} = 92$. The delta and gradient symbols represent the $Re_{\tau 0} = 180$ cases and the $Re_{\tau 0} = 396$ cases, respectively.

Figures 3(a) and 3(b) show the variations of DR and DR_{loss}/DR_{osci} as a function of the inner scale slip length, respectively. The drag reduction properties of the $Re_{\tau 0} = 180$ cases and the $Re_{\tau 0} = 396$ cases are basically the same. As shown in Fig. 3(a), when the isotropic slip length is small enough (e.g., $l_b^{+0} < 1$), the contribution of the streamwise slip length to drag reduction is insufficient to offset the adverse effect of the same slip length in the spanwise direction, as the spanwise slip length can lead to drag increase [16,25]. Busse *et al.* [25] concluded that there is a threshold of streamwise slip length $L_{x,\text{thresh}}^{+0} = 3.5$, greater than which the adverse effect of any spanwise slip length on the skin-friction drag can be ignored. However, as the slip length is very small, the change of the overall drag reduction is weak, i.e., $DR_{loss} \approx 0$. As the slip length increases, the value of DR_{coup} gets closer to DR_{slip}. When the slip length is greater than a certain value (e.g., $l_b^{+0} > 50$), the coupled wall motion can hardly improve the drag reduction, $DR_{loss} \approx DR_{osci}$. Thus, $0 < DR_{loss}/DR_{osci} < 1$, as shown in Fig. 3(b). The tendency of DR_{coup} constantly approaching DR_{slip} can be explained by the coupling phenomenon, which will be described in Sec. III B.

Figure 4(a) shows the variation of DR_{coup} versus the slip length l_b^{+0} and the wall-velocity amplitude I_m^{+0} with a fixed oscillation period $T^{+0} = 92$. Figure 4(b) shows the variation of DR_{coup} versus the slip length l_b^{+0} and the oscillation period T^{+0} with a fixed wall-velocity amplitude $I_m^{+0} = 12$. When the slip length is small, the optimal oscillation period is basically the same as the value under the no-slip boundary condition, i.e., $T^{+0} \approx 100$, and the drag reduction is positively
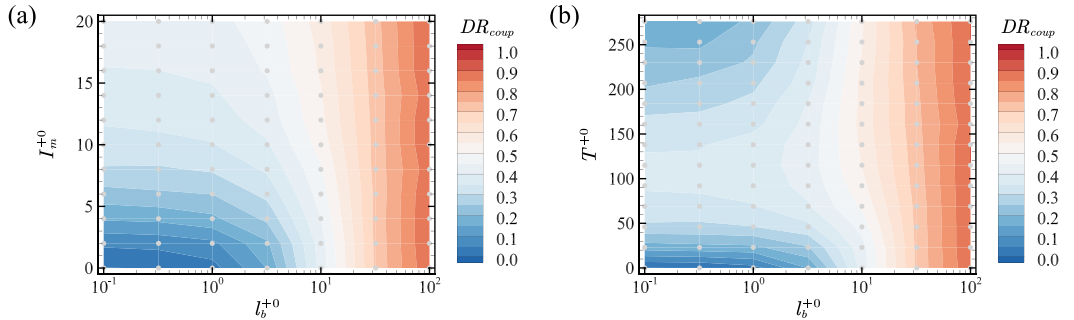

FIG. 4. Contour lines of DR_{coup} versus the slip length l_b^{+0} and (a) I_m^{+0}, (b) T^{+0}. The dots represent the DNS cases, and their parameters are listed in Table II. Case $Re_{\tau 0} = 180$.
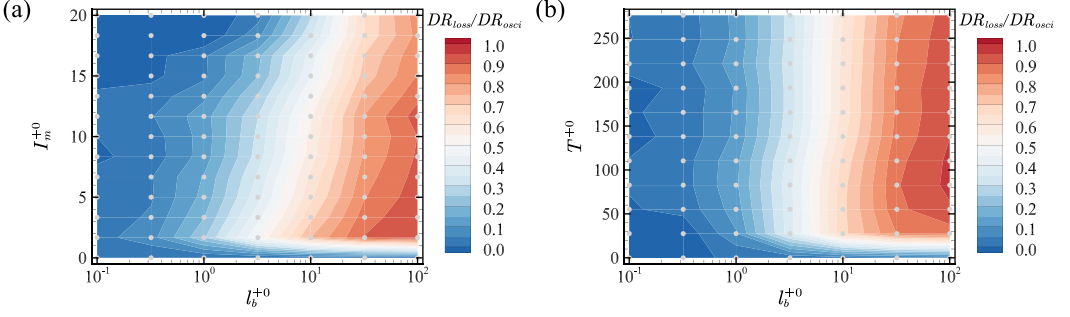
FIG. 5. Contour lines of DR_{loss}/DR_{osci} versus the slip length l_b^{+0} and (a) I_m^{+0}, (b) T^{+0}. The dots represent the DNS cases, and their parameters are listed in Table II. Case $Re_{\tau 0} = 180$.

correlated with the wall-velocity amplitude. As the slip length increases, the contribution of the oscillatory wall motion to the drag reduction becomes weaker, and the influences of the oscillation amplitude and period gradually fade away. The overall trend is that as the slip length increases, the drag reduction gradually changes from the oscillation dominated to the slip dominated.

Figure 5(a) shows the variation of DR_{loss}/DR_{osci} versus l_b^{+0} and I_m^{+0} with $T^{+0} = 92$. Figure 5(b) shows the variation of DR_{loss}/DR_{osci} versus l_b^{+0} and T^{+0} with $I_m^{+0} = 12$. Under the same slip length and oscillation period, the drag reduction loss corresponding to the small wall-velocity amplitude is larger than that of the high wall-velocity amplitude. There are three reasons for this property. The first is that the drag reduction is positively correlated with I_m^{+0}. The second is that the drag reduction as a function of the amplitude changes faster when I_m^{+0} is small, which can be seen from Fig. 8(a) in Sec. III B. The third is that, under a constant oscillation period, the same slip length will lead to the same proportion of amplitude reduction, which will be proved by Eq. (14) in Part B. Hence, under the same T^{+0}, the drag reduction loss corresponding to the small I_m^{+0} should be larger than that of the high I_m^{+0}. The feature shown in Fig. 5(b) is that the drag reduction loss is basically independent of the oscillation period under the same slip length and wall-velocity amplitude.

B. Coupling phenomenon

The results of the numerical simulations reveal that the maximum spanwise velocity of the fluid on the wall caused by the oscillatory wall motion will decrease as the slip length increases, which presents a coupling phenomenon under the coupled boundary condition. This phenomenon can be reflected by the variations of the phase-averaged spanwise velocity, as shown in Fig. 6.
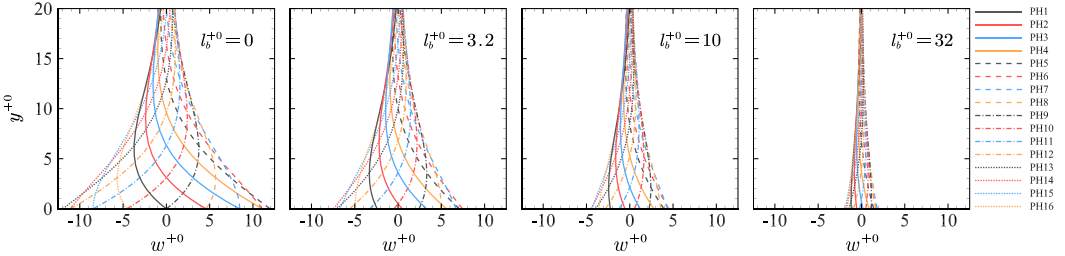

FIG. 6. The phase-averaged spanwise velocity of the fluid on the wall when $l_b^{+0} = 0, 3.2, 10, 32$, respectively. w^{+0} is the spanwise velocity of the fluid scaled with $u_{\tau 0}$. The oscillation parameters of the cases are $I_m^{+0} = 12$ and $T^{+0} = 184$. "PH1" and "PH16" stand for phase $\pi/8$ and 2π, respectively. The interval between adjacent phases is $\pi/8$. Case $Re_{\tau 0} = 180$.

Theoretical interpretation can be obtained through the solution of the flow caused by oscillating plates (i.e., Stokes's second problem). In the spanwise direction of the Stokes layer generated by oscillatory wall motion, the N-S equation can be simplified to the heat conduction equation:

$$\frac{\partial w}{\partial t} = v \frac{\partial^2 w}{\partial y^2}. \tag{8}$$

In addition to the oscillation velocity of the wall, the slip velocity related to the local shear rate should also be considered in the boundary condition:

$$w(y,t) = I_m \sin \omega t + l_b \frac{\partial w}{\partial n}, \quad at \quad y = \pm h, \tag{9}$$

For the simulation parameters in this paper, there is no interference between the Stokes layers on the upper and lower walls. Thus, considering the lower half channel, the general solution of Eq. (8) can be written as:

$$w(y,t) = A e^{-\eta} \sin(\omega t - \eta - \varphi), \tag{10}$$

where φ is the lag phase, $\eta = k(y+h)$, and $k = \sqrt{\omega/2v}$ is the wave number of the oscillation. The normal derivative of the general solution can be written as:

$$\frac{\partial w}{\partial y} = -Ake^{-\eta} \sin(\omega t - \eta - \varphi) - Ake^{-\eta} \cos(\omega t - \eta - \varphi). \tag{11}$$

Substituting Eqs. (10) and (11) into the boundary condition Eq. (9),

$$A \sin(\omega t - \varphi) = I_m \sin \omega t - Akl_b \sin(\omega t - \varphi) - Akl_b \cos(\omega t - \varphi), \tag{12}$$

thereby

$$A = \frac{I_m}{\sqrt{1 + 2kl_b + 2k^2 l_b^2}}, \quad \varphi = \arctan \frac{kl_b}{1 + kl_b}. \tag{13}$$

Let $kl_b = \xi$, then

$$w(y,t) = \frac{I_m}{\sqrt{1 + 2\xi + 2\xi^2}} e^{-\eta} \sin \left(\omega t - \eta - \arctan \frac{\xi}{1+\xi} \right). \tag{14}$$

Equation (14) is the solution of the Stokes's second problem when the wall has a slip length in the oscillation direction.

The wall slip changes both the maximum spanwise velocity and the phase of the fluid on the wall but does not influence the oscillation period. Under a constant oscillation period, the same slip length will lead to the same proportion of amplitude reduction. Figures 7(a) and 7(b) show the comparison of the maximum spanwise velocity and the phase between the DNS results and the Stokes theoretical solution Eq. (14), respectively. As can be seen from Fig. 7(a), the maximum spanwise velocity of the fluid on the wall as a function of the slip length is in good agreement with the Stokes theoretical solution. As shown in Fig. 7(b), the phases of the Stokes flow can be well overlapped after superimposing the lag phases caused by wall slip on the actual phases of the DNS results.

In order to evaluate the drag reduction loss caused by the decrease of the maximum spanwise velocity of the fluid on the wall, define DR_{loss}^{osci} as the drag reduction loss corresponding to this decrease only, i.e., $DR_{loss}^{osci}(I_m^{+0}, T^{+0}, l_b^{+0}) = DR_{osci}(I_m^{+0}, T^{+0}) - DR_{osci}^{eq}(w_{max}^{+0}, T^{+0})$, where DR_{osci}^{eq} is the drag reduction of the spanwise oscillation boundary condition with the wall-velocity amplitude equal to the maximum spanwise velocity of the fluid on the wall w_{max}^{+0} when $l_b \neq 0$. According to Quadrio et al. [42], for a given T^{+0}, the drag reduction will decrease monotonically with the decrease of I_m^{+0}. Figure 8(a) shows the DNS results of DR_{osci} at $T^{+0} = 92$ in the present study and their fitting curve versus I_m^{+0}. For verification, the DNS results from Quadrio et al. [42] are also
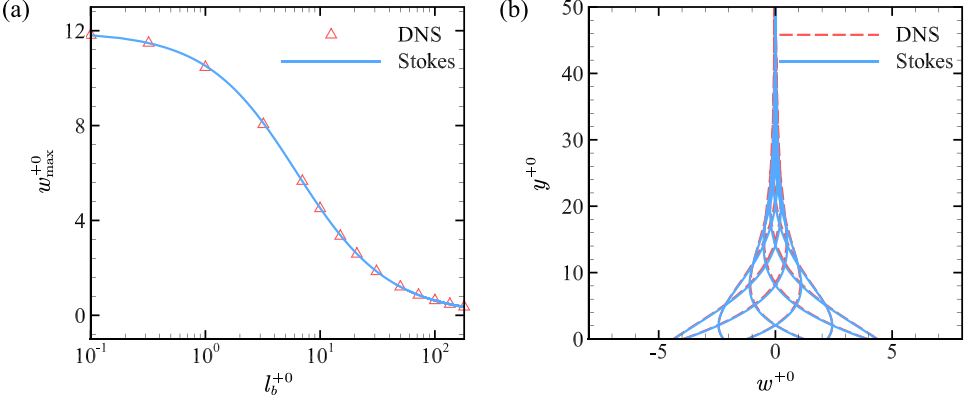
FIG. 7. (a) The maximum spanwise velocity of the fluid on the wall $w_{\max}^{+0}$ versus the slip length l_b^{+0} ($I_m^{+0} = 12$, $T^{+0} = 184$). (b) The DNS results coincide with the Stokes theoretical solution after superimposing the lag phases φ ($l_b^{+0} = 10$). Case $\mathrm{Re}_{\tau 0} = 180$.

plotted in this figure. Figure 8(b) shows the drag reduction loss as a function of the slip length by taking the spanwise oscillation of $I_m^{+0} = 20$ and $T^{+0} = 92$ as the reference ($l_b^{+0} = 0$). In general, the actual drag reduction loss $\mathrm{DR}_{\mathrm{loss}}$ is greater than $\mathrm{DR}_{\mathrm{loss}}^{\mathrm{osci}}$, indicating that the drag reduction of wall slip in the oscillatory turbulent channel flow also decreases, which can be seen from the analysis in Sec. III C.

C. Drag reduction decomposition

In this section, the drag reduction is decomposed according to the contributions arising from different sources. When the spanwise oscillation dominates the drag reduction of the coupled boundary condition, the variation of drag reduction with the oscillation parameters is basically the same as that without slip. Therefore, Sec. III C only focuses on the drag reduction property of slip length under the constant oscillation parameters.

Define the relative drag reduction as $\mathrm{DR}_r = (\langle C_f \rangle_{\mathrm{ref}} - \langle C_f \rangle)/\langle C_f \rangle_{\mathrm{ref}}$, $\langle C_f \rangle_{\mathrm{ref}}$ is the mean friction coefficient of the reference flow when $l_b = 0$. For the slip flow without oscillation, the turbulent baseline flow is used as the reference; for the flow under the coupled boundary condition, the no-slip
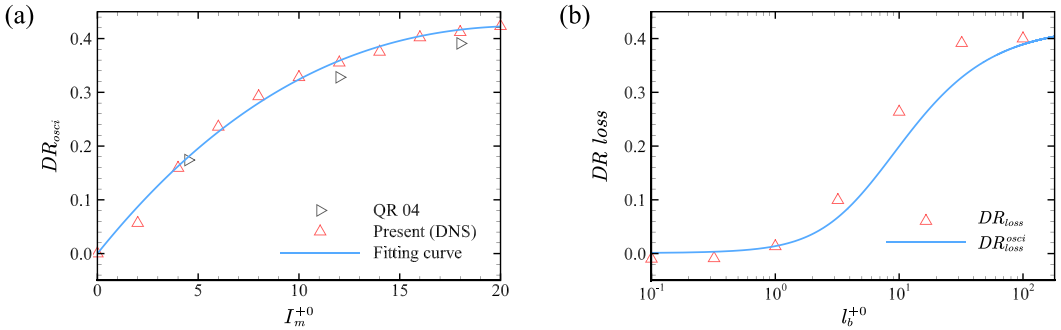

FIG. 8. (a) The DNS results of $\mathrm{DR}_{\mathrm{osci}}$ in the present study and their fitting curve versus I_m^{+0} when $T^{+0} = 92$. The fitting function is $\mathrm{DR}_{\mathrm{osci}} \times 100 = 0.0015(I_m^{+0})^3 - 0.1577(I_m^{+0})^2 + 4.6666(I_m^{+0})$. "QR 04" represent the DNS result of Quadrio et al. [42] at $T^{+0} = 100$, and $\mathrm{Re}_{\tau 0} = 200$. (b) Drag reduction loss $\mathrm{DR}_{\mathrm{loss}}$ and $\mathrm{DR}_{\mathrm{loss}}^{\mathrm{osci}}$ versus l_b^{+0}. Case $\mathrm{Re}_{\tau 0} = 180$.

oscillatory turbulent flow with the same oscillation parameters is used as the reference. For the purposes of the following analysis, a proportionality coefficient ζ is defined to describe the variation of the streamwise pressure gradient,

$$\zeta = \left.\frac{\partial \langle p \rangle}{\partial x}\right|_{\text{slip}} \Bigg/ \left.\frac{\partial \langle p \rangle}{\partial x}\right|_{\text{ref}}, \tag{15}$$

where $\zeta \equiv 1 - \text{DR}_r$, $\partial \langle p \rangle / \partial x|_{\text{slip}}$ is the mean streamwise pressure gradient driving the channel flow when $l_b \neq 0$, and $\partial \langle p \rangle / \partial x|_{\text{ref}}$ is the reference mean pressure gradient without slip.

In laminar Poiseuille flow, the governing equation is

$$-\frac{1}{\rho}\frac{dp}{dx} + \nu \frac{d^2 u}{dy^2} = 0. \tag{16}$$

Note that $dp/dx < 0$. Considering the slip velocity $u(\pm h) = l_b du/dn|_{\pm h}$ on the upper and lower walls, we have

$$u(y) = -\frac{1}{2\mu}\frac{dp}{dx}(h^2 - y^2) - l_b \frac{h}{\mu}\frac{dp}{dx}, \tag{17}$$

where $\mu = \rho \nu$ is the kinetic viscosity. Keeping the flow rate as $2q$, the expression of $dp/dx|_{\text{slip}}$ can be written as $(3q\mu)/(-h^3 - 3h^2 l_b)$. Taking the pressure gradient of the laminar Poiseuille flow under the no-slip boundary condition as the reference, the expression of ζ for the laminar Poiseuille flow is $\zeta = 1/(1 + 3l_b^*)$. Besides, according to the experimental research conducted by Choi and Kim [3], the drag reduction of a laminar Couette flow with one slip surface also has the form of $1/(1 + l_b^*)$, which brings the following question. Is there a similar form for ζ in the turbulent channel flow?

To figure out this unified expression, considering the nonlinearity of turbulence, we define ζ in the turbulent flow as:

$$\zeta = \frac{1}{1 + C(l_b^*)l_b^*}, \tag{18}$$

where the coefficient $C(l_b^*)$ is a function of the slip length.

In the turbulent channel flows, including the turbulent baseline flow and the oscillatory turbulent flow, the DNS results show that $u_s = \langle u \rangle|_{\pm h} = l_b \langle \partial u / \partial n \rangle|_{\pm h}$ is still valid. From a generalization perspective, similar to Fukagata *et al.* [16], the mean velocity profile can be decomposed as Eq. (19) after the actual mean streamwise pressure gradient $\partial \langle p \rangle / \partial x|_{\text{slip}}$ is extracted out,

$$\langle u(l_b, y) \rangle = -\left.\frac{\partial \langle p \rangle}{\partial x}\right|_{\text{slip}} \left[\langle f(l_b, y) \rangle + l_b \left.\frac{\partial \langle f(l_b, y) \rangle}{\partial n}\right|_{\pm h} \right], \tag{19}$$

where $\langle f(l_b, \pm h) \rangle = 0$ and $\partial \langle f(l_b, y) \rangle / \partial n|_{\pm h}$ is derived from the slip boundary condition. Equation (19) shows that the mean velocity profile can be decomposed into two parts, which is illustrated in Fig. 9.

For the no-slip reference flow,

$$\langle u(0, y) \rangle = -\left.\frac{d \langle p \rangle}{dx}\right|_{\text{ref}} \langle f(0, y) \rangle. \tag{20}$$

Under the constant flow rate condition, there is

$$-\left.\frac{d \langle p \rangle}{dx}\right|_{\text{ref}} \int_0^h \langle f(0, y) \rangle dy = -\left.\frac{d \langle p \rangle}{dx}\right|_{\text{slip}} \int_0^h \left[\langle f(l_b, y) \rangle + l_b \left.\frac{\partial \langle f(l_b, y) \rangle}{\partial n}\right|_{\pm h} \right] dy. \tag{21}$$
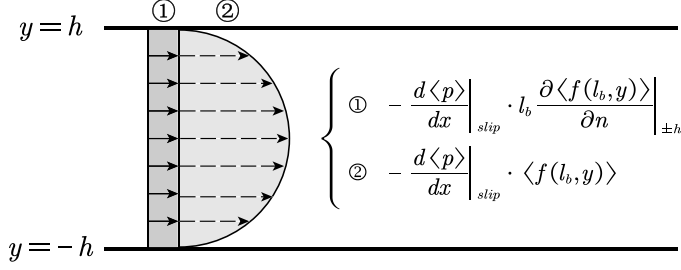
FIG. 9. Decomposition of the mean velocity profile in turbulent channel flow. ① represents the mean slip velocity on the wall, i.e., u_s. ② is the remaining part after deducting u_s from the mean velocity profile, and ② is zero on the wall.

Therefore,

$$\zeta = \int_0^h \langle f(0,y) \rangle dy \bigg/ \int_0^h \left[\langle f(l_b, y) \rangle + l_b \frac{\partial \langle f(l_b, y) \rangle}{\partial n} \bigg|_{\pm h} \right] dy. \tag{22}$$

According to Eq. (18), there is $C(l_b^*) = (1 - \zeta)/l_b^* \zeta$. Substituting Eq. (22) into this relation, we have

$$C(l_b^*) = \underbrace{h^2 \frac{\partial \langle f(l_b, y) \rangle}{\partial n} \bigg|_{\pm h} \bigg/ \int_0^h \langle f(0,y) \rangle dy}_{C_1(l_b^*)} + \underbrace{\left[\int_0^h \langle f(l_b, y) \rangle dy \bigg/ \int_0^h \langle f(0,y) \rangle dy - 1 \right] \bigg/ l_b^*}_{C_2(l_b^*)}, \tag{23}$$

and name the two terms on the right-hand side as $C_1(l_b^*)$ and $C_2(l_b^*)$, respectively.

Combining the expressions for ζ and $C_1(l_b^*)$ [Eqs. (22) and (23)], and $u_s = l_b \langle \partial u/\partial n \rangle|_{\pm h}$, we can get that $C_1 l_b^* \zeta = u_s/U_b$. Furthermore, ζ is also equal to $\langle \tau_w^{\text{slip}} \rangle / \langle \tau_w^{\text{ref}} \rangle$, where $\langle \tau_w^{\text{slip}} \rangle = \mu \langle \partial u(l_b, y)/\partial n \rangle|_{\pm h}$ is the mean wall shear stress when $l_b \neq 0$, and $\langle \tau_w^{\text{ref}} \rangle = \mu \langle \partial u(0, y)/\partial n \rangle|_{\pm h}$ is the mean wall shear stress of the no-slip reference flow. Therefore, $C_1(l_b^*)$ can also be expressed as

$$C_1(l_b^*) = \frac{u_s}{U_b l_b^* \zeta} = \frac{h}{U_b} \frac{\partial \langle u(0,y) \rangle}{\partial n} \bigg|_{\pm h} = \frac{h}{\mu U_b} \langle \tau_w^{\text{ref}} \rangle. \tag{24}$$

Thus, C_1 is a constant which is independent of the slip length. In the slip flow, C_1 remains consistent with the value of the no-slip reference flow. Since the above decomposition starts from the mean velocity profile and takes the flow without slip as the reference, it is applicable to both the turbulent baseline flow and the oscillatory turbulent flow.

The relationship between C_1, $C_2(l_b^*)$ and DR_r, ζ is

$$\text{DR}_r \equiv 1 - \zeta = [C_1 + C_2(l_b^*)]l_b^* \zeta = \frac{u_s}{U_b} + C_2(l_b^*)l_b^* \zeta. \tag{25}$$

As constituents of $C(l_b^*)$, C_1, and $C_2(l_b^*)$ represent two sources of the drag reduction. Compared to the expression of Rastegari *et al.* [26], the decomposition of $C(l_b^*)$ in the current work has the same meaning as their expression $\text{DR} = u_s/U_b + O(\varepsilon)$. C_1/C and $C_2(l_b^*)/C$ represent the proportions of the contributions to the drag reduction (or drag increase) resulting from the effective slip on the wall and the modifications to the turbulent dynamics, respectively. The DNS results of C_1 and C_2, as well as C_2/C_1 are shown in Fig. 10. Hereafter, C_2 is short for $C_2(l_b)$. C_2/C_1 describes the ratio of the contribution from the modifications of turbulent dynamics to the contribution from the effective slip on the wall. For validation, the DNS results of Min *et al.* [23] and Busse *et al.* [25] are also shown in Fig. 10. As can be seen from Figs. 10(a) and 10(c), the absolute value of C_2 is much
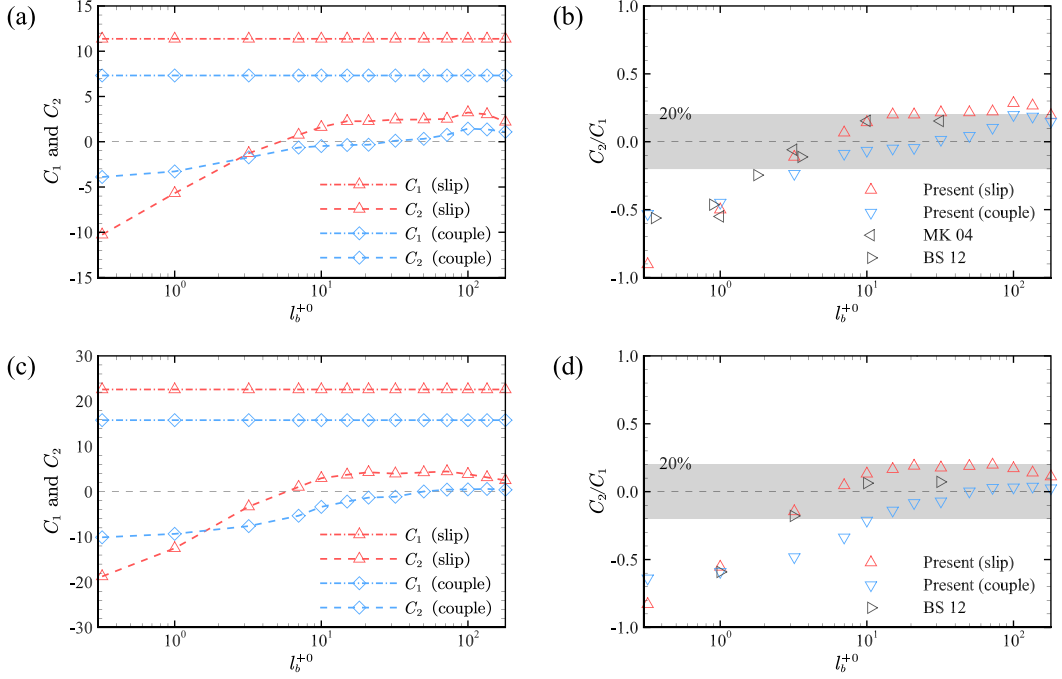
FIG. 10. The DNS results of [(a) and (c)] C_1, C_2, and [(b) and (d)] C_2/C_1 versus the inner scale slip length l_b^{+0}. "slip" represents the flow under the isotropic slip boundary condition. "couple" represents the flow under the coupled boundary condition with $I_m^{+0} = 12$ and $T^{+0} = 92$. Panels (a) and (b) are the results of the cases of $\mathrm{Re}_{\tau 0} = 180$. Panels (c) and (d) are the results of the cases of $\mathrm{Re}_{\tau 0} = 396$. In (b), "MK 04" and "BS 12" represent the DNS results of Min *et al.* [23] and Busse *et al.* [25] (isotropic slip boundary condition, $\mathrm{Re}_{\tau 0} = 180$), respectively. In (d), "BS 12" represents the DNS result of Busse *et al.* [25] (isotropic slip boundary condition, $\mathrm{Re}_{\tau 0} = 360$). The way to calculate C_1 and C_2 of Refs. [23,25] is $C_1 = h\langle\tau_w^{\mathrm{ref}}\rangle/\mu U_b$ and $C_2(l_b^*) = \mathrm{DR}_r/l_b^*\zeta - C_1$.

smaller than the constant C_1 after the slip length exceeds a certain value. In addition, the value of C_1 under the coupled boundary condition is smaller than that under the isotropic slip boundary condition, which proves that the drag reduction of the same slip length in the oscillatory turbulent flow is lower than that in the turbulent baseline flow. As shown in Figs. 10(b) and 10(d), for the turbulent baseline flow, the contribution from the modifications of turbulent dynamics to the drag increase is large when the isotropic slip length is small, e.g., when $l_b^{+0} = 1$, C_2/C_1 is around -50%. As the slip length increases, this proportion gradually changes to around 20%, and the effect of C_2 changes from drag increase to drag reduction. Additionally, compared with the turbulent flow without oscillation, the critical slip length which makes the contribution of the modifications of turbulent dynamics change from drag increase to drag reduction increases in the oscillatory turbulent flow.

In summary, compared with the respective no-slip reference flow, the proportionality coefficients ζ of laminar (including the laminar Couette flow and the laminar Poiseuille flow) and turbulent channel flows (including the turbulent baseline flow and the oscillatory turbulent flow) are demonstrated to be in a unified form [i.e., Eq. (18)] versus the outer scale slip length. For laminar flow, C is a constant. For turbulent flow, C is composed of C_1 and C_2, and C_1 remains consistent with the value of the no-slip reference flow. The contribution from the modifications of turbulent dynamics represented by C_2 will undergo a shift from drag increase to drag reduction as the isotropic slip length increases.

TABLE III. Abbreviation of case name and the corresponding parameters. Case $Re_{\tau 0} = 180$.

Abbr	I_m^{+0}	T^{+0}	l_b^{+0}	DR
Base	0	0	0	0
Slip	0	0	7	0.31
Osci	12	184	0	0.31
Coup	12	184	7	0.50

IV. COUPLING EFFECT ON WALL TURBULENCE

In this section, the coupling effect of the coupled boundary condition on the turbulent dynamics will be addressed. The time-averaged results, including the mean velocity profiles and the second moments, as well as the empirical mode decomposition (EMD) of the friction coefficient are conducted in Sec. IV A. The quadrant analysis of the production term of the turbulent kinetic energy (TKE), and the joint probability density function (PDF) of u' and v', are carried out in Sec. IV B. The phase-averaged variations of the turbulence properties during the oscillation period are shown in Sec. IV C. Finally, in Sec. IV D, the variation of the inclination angle of the streaks is analyzed based on the phase-averaged two-point correlation function of the streamwise velocity fluctuations.

The analysis in this section is mainly based on four cases of $Re_{\tau 0} = 180$ under different boundary conditions. In what follows, unless otherwise noted, the turbulent baseline flow is represented by "*Base*," the isotropic slip boundary condition is indicated by "*Slip*," "*Osci*" is used to represent the spanwise oscillation boundary condition, and "*Coup*" indicates the coupled boundary condition. The specific parameters of the four cases are shown in Table III. For the validity of the comparison, the drag reduction of the selected "*Slip*" case and the "*Osci*" case are close to each other.

A. Turbulence statistics

Figures 11(a) and 11(b) show the mean velocity profiles of $\langle u^+ \rangle$ and $\langle u^+ \rangle - \langle u_s^+ \rangle$, respectively. In both figures, the delta symbols represent the DNS results under the isotropic slip boundary condition conducted by Min *et al.* [23], and their condition is $Re_{\tau 0} = 180$ and $l_b^{+0} = 3.566$. The diamond symbols represent the DNS results under the spanwise oscillation boundary condition conducted by Touber *et al.* [43], and the corresponding condition is $Re_{\tau 0} = 200$, $I_m^{+0} = 12$, and $T^{+0} = 100$. The results in the current work are slightly different from those in the literature due to the different
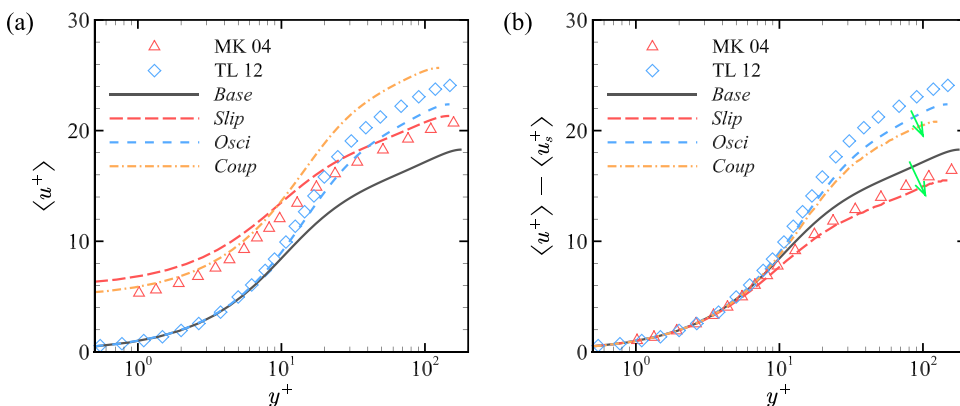

FIG. 11. Mean velocity profiles (a) $\langle u^+ \rangle$ and (b) $\langle u^+ \rangle - \langle u_s^+ \rangle$ in wall units scaled with the actual friction velocity. "MK 04" and "TL 12" represent the DNS results of Min *et al.* [23] (the isotropic slip boundary condition) and Touber *et al.* [43] (the spanwise oscillation boundary condition), respectively.
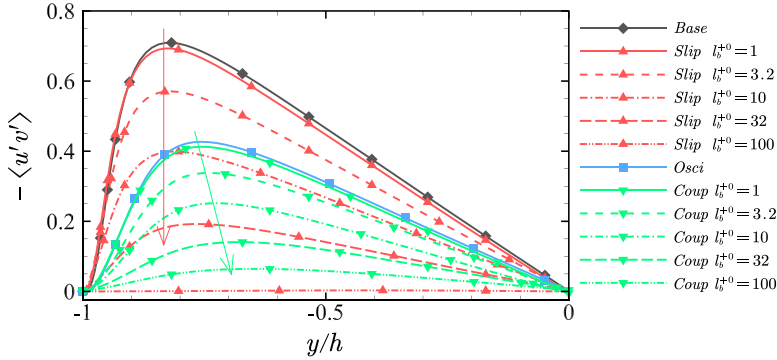
FIG. 12. The Reynolds shear stress $-\langle u'v'\rangle$ normalized by $u_{\tau 0}^2$ in global coordinates. $y/h = -1$ represents the lower wall of the channel. The red lines represent the results under the isotropic slip boundary condition, and the green lines represent the results under the coupled boundary condition with $I_m^{+0} = 12$ and $T^{+0} = 184$. The arrows in the figure indicate the change of the peak position of the Reynolds shear stress as the slip length increases.

simulation parameters, but the variation trend of the mean velocity profiles under the isotropic slip boundary condition and the spanwise oscillation boundary condition is consistent with that in the literature.

As can be seen from Fig. 11(a) of the time-averaged velocity profiles, on the one hand, the effective wall slip (the "*Slip*" case) increases the mean streamwise velocity in the near-wall region, and the slope of the log layer is almost the same as the turbulent baseline flow. On the other hand, the oscillatory wall motion (the "*Osci*" case) which generates a Stokes layer thickens the viscous sublayer, and then lead to the elevation of the buffer and log layers. As a result, the coupled boundary condition mixes the above effects, and the slope of the log layer is almost the same as the slope when only the oscillatory wall motion is applied. After subtracting the respective time-averaged streamwise slip velocity $\langle u_s^+\rangle$ on the wall, the profiles collapse in the viscous sublayer, and another two obvious characteristics can also be seen from Fig. 11(b). The first characteristic is that the velocity profiles are similar before and after the application of wall slip, nothing but the log layer is shifted downward. The slope is basically unchanged, regardless of that the slip is applied on the turbulent baseline flow or the oscillatory turbulent flow. The second characteristic is that the shift of the outer layer caused by the slip acting on the oscillatory turbulent flow is obviously smaller than that of the turbulent baseline flow. These two characteristics are well correlated with the change of the statistical properties. The first characteristic shows that the influence of slip on turbulent dynamics is limited, which can be seen from the analyses of the turbulence properties in the following sections. The second characteristic reflects that the same isotropic slip length has a weaker effect on the oscillatory turbulent flow than the turbulent baseline flow. This can also be supported by the fact that the relative drag reduction of the same slip length acting on the oscillatory turbulent flow is less than that of the turbulent baseline flow.

The distribution of $-\langle u'v'\rangle$ throughout the entire channel height is shown in Fig. 12. As the isotropic slip length increases, the Reynolds shear stress becomes smaller and smaller throughout the channel. According to Busse *et al.* [25], the increasing slip length will promote the process of relaminarization, and the decay of Reynolds shear stress is one of the features of relaminarization [48]. Under the isotropic slip boundary condition, when $l_b^{+0} = 100$, $-\langle u'v'\rangle$ in the channel almost disappears. However, when $l_b^{+0} = 100$, the Reynolds shear stress in the oscillatory turbulent flow is obviously higher than that in the slip flow without oscillation. This reflects an unexpected property that the existence of the Stoke layer delays the relaminarization process caused by the large slip length. Nevertheless, under the coupled boundary condition, the Reynolds shear stress will still disappear as the slip length increases, which can be seen from the variation trend. Of course, this

critical slip length depends on the oscillation parameters. Figure 11(b) has shown that the same slip length has a weaker ability to change the mean velocity profile of the oscillatory turbulent flow, compared to the turbulent baseline flow. Therefore, the existence of the stokes layer will mitigate the influence of wall slip on turbulent fluctuations. The peak position of Reynolds shear stress remains basically unchanged under the isotropic slip boundary condition (a similar trend can be seen from Min *et al.* [23]), while the peak position is pushed outward under the coupled boundary condition, as indicated by the arrows in Fig. 12. This is because the coupled boundary condition has a stronger inhibition on the ejection events than before coupling. It can be seen clearly from the quadrant analysis in Sec. IV B.

According to Rastegari *et al.* [26], the friction coefficient of channel flow with wall slip can be expressed as:

$$C_f = \frac{6}{\text{Re}_b}\left(1 - \frac{u_s}{U_b}\right)\left(\frac{1}{1 - 3I^+}\right), \tag{26}$$

where $I^+ = \int_0^h y[-\langle u'v'\rangle^+ - \langle\bar{u}\bar{v}\rangle^+]dy$ (the upper half channel). There is no secondary mean flow under the isotropic slip boundary condition, leading to that $\langle\bar{u}\bar{v}\rangle = 0$. In the laminar flow, $I^+ = 0$. The integral of the weighted Reynolds shear stress in the normal direction represents the contribution of turbulent fluctuations to the total friction coefficient. Figure 13(a) is the comparison of the weighted Reynolds shear stress $-y\langle u'v'\rangle$ under different boundary conditions. Compared with the "*Osci*" case, the wall slip of the coupled boundary condition condenses the envelope range of the phase fluctuations caused by the oscillatory wall motion, and further suppresses the generation of the Reynolds shear stress. More details about the Reynolds stress transport are presented in Sec. IV C. Figures 13(b), 13(c) and 13(d) are the comparison of the RMS velocity fluctuations of the streamwise, wall-normal, and spanwise directions, respectively. The streamwise and spanwise RMS velocity fluctuations in the viscous sublayer increase visibly due to the wall slip, and the envelope range of their phase fluctuations caused by the periodic oscillation also increases in this region. However, as v' is weak in the viscous sublayer and the cross-correlation between u' and v' is reduced, the phase fluctuation of $-y\langle u'v'\rangle$ is not greatly affected in this region. The reduced cross-correlation between u' and v' fluctuations can be reflected by the joint PDF in Sec. IV B, as shown in Fig. 16. In the buffer and log layers, the envelope ranges of the RMS velocity fluctuations decrease under the coupled boundary condition. As a result, the magnitude of the periodic fluctuations of the friction coefficient will also decrease, which is shown in Fig. 14. Here, the periodic fluctuations are the phase-averaged results of the wall-averaged friction coefficient.

Figure 14(a) shows the temporal variations of the wall-averaged friction coefficients of the four cases. The EMD method [45,49], part of the Hilbert-Huang transform (HHT), which can generate a collection of intrinsic mode functions (IMF), is used to distinguish the large-scale components and the small-scale fluctuations of the wall-averaged friction coefficient. The EMD method can be expressed as

$$X(t) = \sum_{i=1}^{n} \text{IMF}_i + r_n, \tag{27}$$

where IMF_i is the ith empirical mode and r_n is the residue. Therefore, the original signal $X(t)$ is decomposed into n empirical modes and a residue. Note that IMF_1 is the highest frequency component. The large-scale components of the wall-averaged friction coefficients of the "*Osci*" case and the "*Coup*" case are also shown in Fig. 14(a), i.e., r_{osci} and r_{coup}, which are the results of deducting the first three ($n = 3$) and first two ($n = 2$) modes from their original signals, respectively. The selection criterion of n is to ensure that $\sum_{i=1}^{n} \text{IMF}_i$ has the same frequency as the spanwise oscillation. The dark gray area in Fig. 14(a) corresponds to a time range from 480 to 800, containing 20 oscillation periods. The deducted components are the small-scale fluctuations of the friction coefficients, i.e., $\sum_{i=1}^{n} \text{IMF}_i$, as shown in Fig. 14(b).
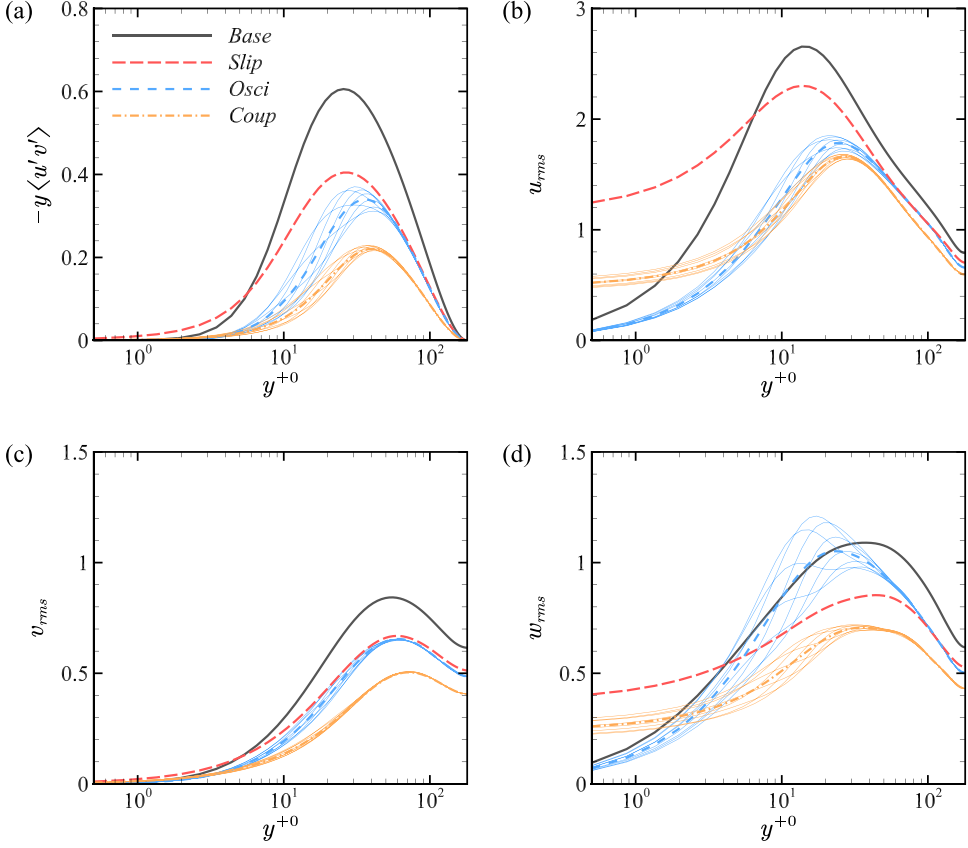
FIG. 13. (a) The weighted Reynolds shear stress $-y\langle u'v'\rangle$ of the upper half channel in wall units scaled with $u_{\tau 0}^2 h$. Panels (b), (c), and (d) are the RMS velocity fluctuations (scaled with $u_{\tau 0}$) of the streamwise, wall-normal, and spanwise directions, respectively. The blue and yellow thin solid lines represent different phases of the "*Osci*" case and the "*Coup*" case, respectively. The thick lines represent the time-averaged results.

The periodic fluctuations of the friction coefficients $\hat{C}_f$ of the "*Osci*" case and the "*Coup*" case are shown in Figs. 14(c) and 14(d), respectively. Sixteen phases in an oscillation period are considered. Compared to the "*Osci*" case, the magnitude of the periodic fluctuations of the friction coefficient pronouncedly decreases in the "*Coup*" case. In Figs. 14(c) and 14(d), the periodic fluctuations calculated from the data with and without large-scale components are roughly the same, which are represented by the thick solid line and the dashed line, respectively. A similar characteristic can be seen in Agostini *et al.* [45]. Moreover, the periodic fluctuations in Fig. 14(c) is of the same magnitude as that of Agostini *et al.* [45], although their friction Reynolds number is as high as 1000. The vertical bars represent the standard deviation $\pm\sigma$ corresponding to the data without large-scale components, i.e., $\sum_{i=1}^{n} \text{IMF}_i$. σ is evaluated from

$$\sigma = \sqrt{\frac{1}{N-1} \sum_{n=1}^{N} [X|_{\phi+(n-1)T} - \tilde{X}|_{\phi}]^2}, \tag{28}$$

where $\phi \in \{0, T\}$, and $N = 20$. For both the "*Osci*" case and the "*Coup*" case, the standard deviation is smaller than the amplitude of the periodic fluctuation of the phase-averaged friction coefficient. The fact that the average results with and without large-scale components are very close indicates
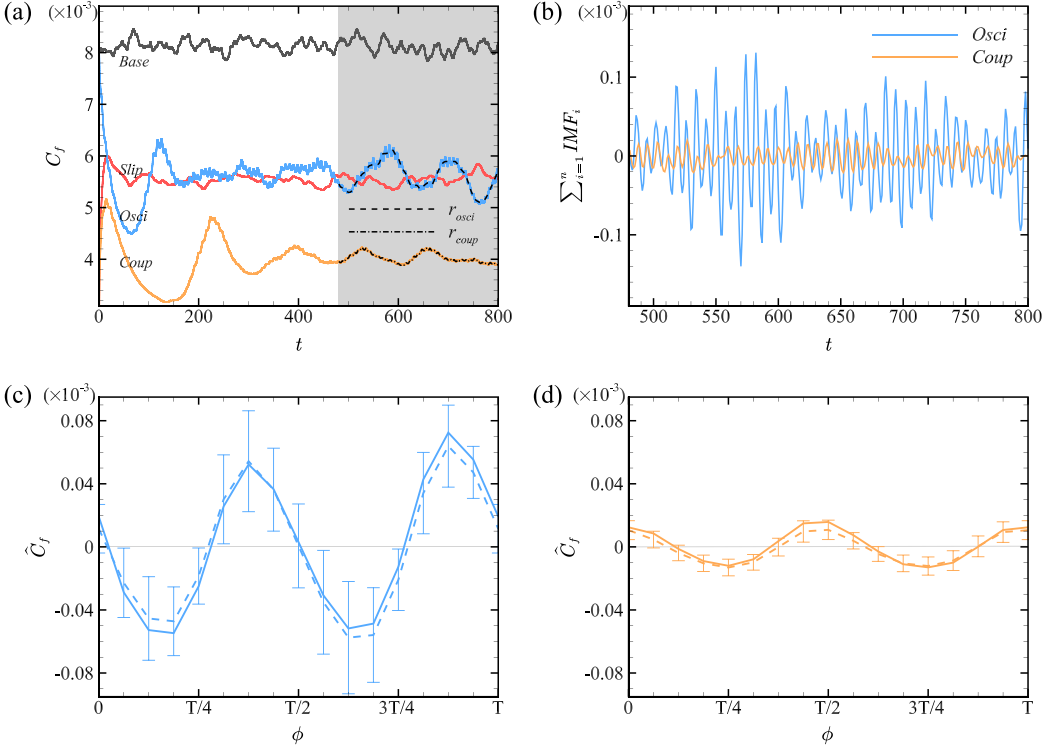
FIG. 14. (a) The temporal variations of the wall-averaged friction coefficients of the four cases (solid lines). The large-scale components of the "*Osci*" case and the "*Coup*" case are represented by r_{osci} (dashed line) and r_{coup} (dash-dot line), respectively. (b) The small-scale fluctuations of the friction coefficients of the "*Osci*" case and the "*Coup*" case. For the "*Osci*" case, $n = 3$. For the "*Coup*" case, $n = 2$. Panels (c) and (d) are the periodic fluctuations of the phase-averaged friction coefficients of the "*Osci*" case and the "*Coup*" case, respectively. The vertical bars represent the standard deviation calculated from the data without large-scale components.

that the error arising from retaining the large-scale components is low. Therefore, in the current work, the operation of removing the large-scale components is not performed in the phase-averaged statistics.

B. Quadrant analysis

In this section, the quadrant analysis will be carried out on the exchange term of the TKE $k = \langle u_i' u_i' \rangle / 2$, followed by the joint PDF of (u', v'). The turbulent exchange term refers to the exchange of physical quantities between the mean flow and the turbulent fluctuations. The exchange term between mean flow kinetic energy and TKE is P_k,

$$P_k = -\langle u_i' u_j' \rangle \frac{\partial \langle u_i \rangle}{\partial x_j}. \tag{29}$$

In the direction of the turbulent flow field where the average strain rate is not zero, part of the energy in the mean flow is transferred to the turbulent fluctuations by the Reynolds stress. P_k is the only source of TKE in the turbulent flow field, also known as the production term. The quadrants are divided according to the signs of u' and v'. The second quadrant ($u' < 0, v' > 0$) contains the ejection events of the turbulent bursting processes, and the fourth quadrant ($u' > 0, v' < 0$) contains
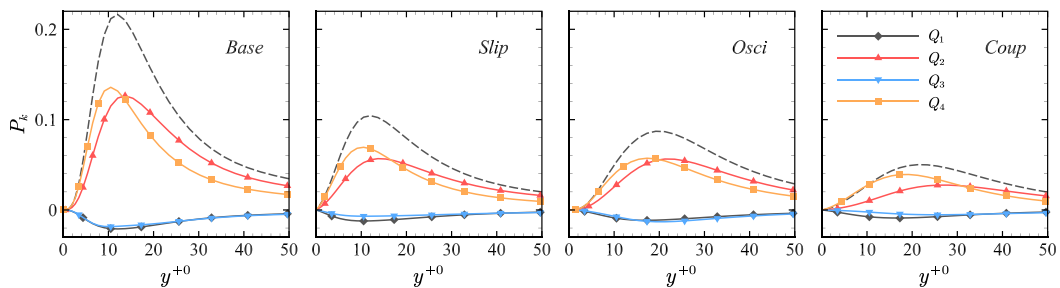
FIG. 15. P_k from each quadrant scaled with $u_{\tau 0}^3/\delta_\nu$ of the turbulent baseline flow. Black long dashed lines are the total P_k of the four quadrants.

the sweep events. The high-speed fluid washing against the wall accompanying with the sweep events are the main source of the high skin-friction drag in wall turbulence.

As can be seen from Fig. 15, the turbulent processes associated with the fluctuations from the second and the fourth quadrants dominate the production of the TKE. Under the isotropic slip boundary condition, the region where the fourth quadrant dominates the production of the TKE is about $y^{+0} < 16$, slightly larger than the turbulent baseline flow (about $y^{+0} < 13$). Within this region, the contribution of the sweep events is greater than that of the ejection events. This is because the velocity and its fluctuations in the near-wall region are small, and the sweep events spurt from the normal position far away from the wall, which contains more energy than the ejection events. The oscillatory wall motion extends the region where the fourth quadrant dominates to $y^{+0} < 20$. This phenomenon indicates that the oscillatory wall motion suppresses the ejection events in the near-wall region to a greater extent than the sweep events, due to that the Stokes layer happens to be the main area where the ejection events occur. In this way, it can be understood that the effective thickness of the Stokes layer is positively correlated with drag reduction [37,42]. Under the coupled boundary condition, the above range is further extended to $y^{+0} < 30$, indicating that the wall slip can enhance the oscillatory wall motion to suppress the ejection events and increase the normal range where the fourth quadrant dominates the production of the TKE.

The TKE mainly comes from the bursting process in the near-wall region. Hence, the decrease in the production indicates that the coupled boundary condition can strongly inhibit this process. Figure 16 compares the joint PDF of u' and v' at $y^{+0} = 10.5$ under different boundary conditions. Compared to the turbulent baseline flow, the isotropic slip slightly narrows the distributions of the second, the third, and the fourth quadrants, the high velocity fluctuations are suppressed, and the highest probability density mainly appears in the fourth quadrant. Also compared with the turbulent baseline flow, there is a strong narrowing when the spanwise wall oscillation is implemented, indicating that the turbulent fluctuations in the Stokes layer are weakened pronouncedly. In addition, under the periodic oscillation, the region with the highest probability density appears to be concentrated on the side of $u' < 0$. When the isotropic slip is applied on the oscillatory turbulent flow, the high wall-normal velocity fluctuations are further suppressed, but the probability of the high streamwise velocity fluctuations are slightly increased, which is different from the effect of slip on the turbulent baseline flow. Another notable feature of the "*Coup*" case is the apparent counterclockwise rotation in the joint PDF compared to the "*Osci*" case, indicating a decrease in the cross-correlation between the streamwise and the wall-normal fluctuations.

C. Phase-averaged properties

In this section, the phase-averaged variations of the turbulence properties during the oscillation period are concerned, including the Stokes strain, the Reynolds normal stresses and the enstrophy budgets. The phasewise variation of the Stokes strain $\widetilde{\partial w/\partial y}$ is shown in Fig. 17. The oblique
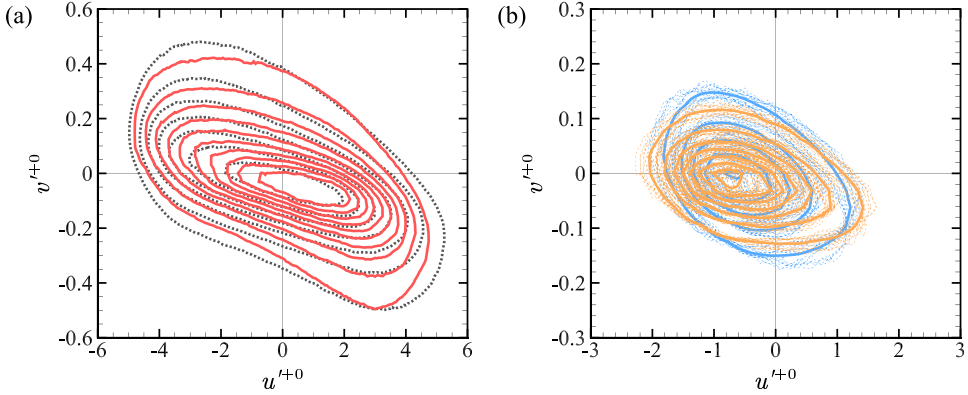
FIG. 16. The joint PDF of u' and v' at $y^{+0} = 10.5$, scaled with $u_{\tau 0}$. (a) The "*Base*" case (black dashed lines) compared with the "*Slip*" case (solid red lines). The probability density in this figure ranges from 100 to 10. (b) The "*Osci*" case (blue lines) compared with the "*Coup*" case (yellow lines), solid lines represent the time-averaged results, and the dotted lines represent the phase-averaged results. The probability density in this figure ranges from 800 to 100.

lines at the intersection of positive and negative strains represent the isolines of zero strain. For the "*Osci*" case, when the spanwise velocity of the wall is zero, the Stokes strain on the wall reaches the extreme value. The phases where the arrows located are the zero-strain phases of the fluid on the wall. For the oscillatory turbulent flow without slip, when the Stokes strain in the upper region of the viscous sublayer (e.g., the region of $5 < y^{+0} < 10$) is high and changes slowly with the phase, the streamwise skin-friction drag will increase. When the Stokes strain near this region is low and changes rapidly, the skin-friction drag will decrease. This is consistent with the observation in the literature [43,45].

When the isotropic slip is applied to the oscillatory turbulent flow (the "*Coup*" case), the magnitude of the Stokes strain is significantly reduced and the phase lags. Another obvious feature is that the phase corresponding to the minimum of the phase-averaged friction coefficient is closer to the zero-strain phase on the wall. According to Eq. (14), when $l_b^{+0} = 7$, the lag phase φ is about 0.4456, which is exactly the difference between the zero-strain phases indicated by the arrows on the same side of Figs. 17(a) and 17(b). Note that T corresponds to the phase 2π. According to the
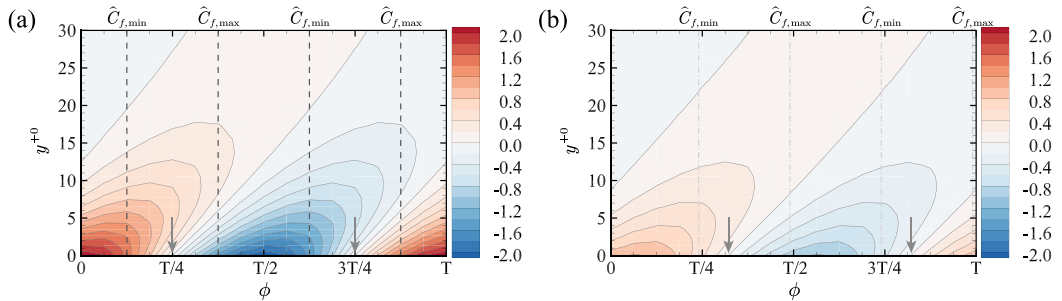

FIG. 17. Contours of the phase-averaged Stokes strain scaled with $u_{\tau 0}/\delta_v$. (a) The "*Osci*" case. (b) The "*Coup*" case. The phases corresponding to the maximum and minimum of the periodic fluctuations of the friction coefficient are also marked with vertical dashed lines in the two figures. The maximum and minimum are obtained by Fourier fitting of the curves shown in Figs. 14(c) and 14(d). 0 and T/2 correspond to the zero-velocity states of the wall.
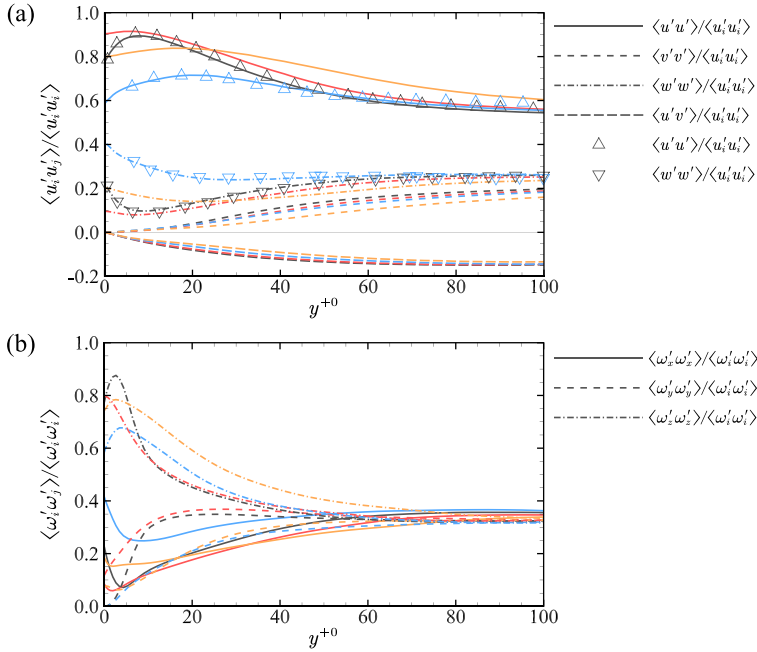
FIG. 18. The distributions of the anisotropy ratio. (a) $\langle u_i' u_j' \rangle / \langle u_i' u_i' \rangle$. (b) $\langle \omega_i' \omega_j' \rangle / \langle \omega_i' \omega_i' \rangle$. In both figures, the line style is used to distinguish different physical quantities. The "*Base*," "*Slip*," "*Osci*," and "*Coup*" cases are distinguished by the black, red, blue, and yellow lines, respectively. In (a), the delta and gradient symbols represent the $\langle u'u' \rangle / \langle u_i' u_i' \rangle$ and $\langle w'w' \rangle / \langle u_i' u_i' \rangle$ of the DNS results from Touber *et al.* [43].

comparison in these two figures, the friction coefficient lags about $T/8$ (the corresponding lag phase is about $\pi/4$), which is obviously larger than the lag phase of the spanwise velocity or the Stokes strain. This is a new phenomenon that is noteworthy. As can be seen from the following analysis, this is caused by the hysteresis of the turbulent dynamics.

Before investigating the budgets, the distributions of the anisotropy ratio are compared. Figures. 18(a) and 18(b) show the ratios of the Reynolds stress components to $\langle u_i' u_i' \rangle$ (twice the TKE) and the ratios of the enstrophy components to $\langle \omega_i' \omega_i' \rangle$, respectively. Note that the enstrophy component refers to one of the three constituents that contribute to the scalar enstrophy. In Fig. 18(a), the delta and gradient symbols represent the $\langle u'u' \rangle / \langle u_i' u_i' \rangle$ and $\langle w'w' \rangle / \langle u_i' u_i' \rangle$ of the DNS results from Touber *et al.* [43], the corresponding condition is $\text{Re}_{\tau 0} = 200$, $I_m^{+0} = 12$, and $T^{+0} = 200$. The black and blue symbols represent the results of the turbulent baseline flow and the oscillatory turbulent flow, respectively. The results of the "*Base*" and the "*Osci*" cases in the current work are in good agreement with the literature [43].

As shown in Fig. 18(a), for the "*Osci*" case, compared with the turbulent baseline flow, the proportion of $\langle u'u' \rangle$ decreases and the proportion of $\langle w'w' \rangle$ increases, while the proportions of $\langle u'v' \rangle$ and $\langle v'v' \rangle$ are basically unchanged. It means that the oscillatory wall motion makes the turbulent energy transfer from the streamwise direction to the spanwise direction. For the "*Coup*" case, the viscous diffusion from the wall is restrained, and the energy transfer from $\langle u'u' \rangle$ to $\langle w'w' \rangle$ is weakened. For $\langle u'v' \rangle$ and $\langle v'v' \rangle$, although their proportions do not change significantly, there is a monotonous trend as shown in Fig. 18(a), that is, the higher the drag reduction, the smaller the absolute values of their ratio. The enstrophy components have a similar property. As shown in Fig. 18(b), for the "*Osci*" case, compared with the turbulent baseline flow, the proportion of $\langle \omega_x' \omega_x' \rangle$ contributes to the enstrophy increases greatly, while the proportions of $\langle \omega_y' \omega_y' \rangle$ and $\langle \omega_z' \omega_z' \rangle$ in the viscous sublayer decrease. For the "*Coup*" case, there is no significant change in $\langle \omega_y' \omega_y' \rangle$,
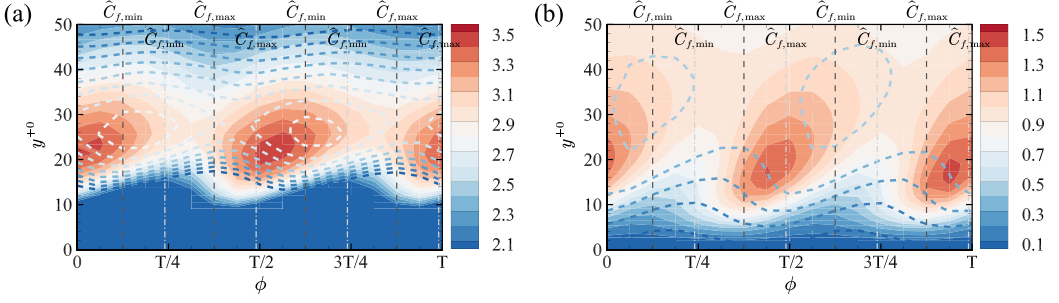
FIG. 19. Contours of the phase-averaged (a) $\widetilde{u'u'}$ and (b) $\widetilde{w'w'}$, normalized by the inner scale of the turbulent baseline flow. The contour maps represent the results of the "*Osci*" case, and the colored contour lines represent the results of the "*Coup*" case, using the same color legend. The vertical dashed lines have the same meaning as in Fig. 17.

but the separation between the streamwise and spanwise fluctuations increases, as the process of transferring energy from $\langle \omega_z' \omega_z' \rangle$ to $\langle \omega_x' \omega_x' \rangle$ is inhibited.

Figures 19(a) and 19(b) show the contours of the phase-averaged $\widetilde{u'u'}$ and $\widetilde{w'w'}$, respectively. For comparison, the results of the "*Osci*" case and the "*Coup*" case are overlapped in one figure. It can be seen that the peak positions of $\widetilde{u'u'}$ and $\widetilde{w'w'}$ are elevated, and their lag phases are basically the same as the lag of the phase-averaged friction coefficient. The elevation of the peak position is due to the strong inhibition of the ejection events by the coupled boundary condition. According to the statistical characteristics of turbulent channel flow, the budgets of the phase-averaged Reynolds stress can be expressed as

$$\frac{\partial \widetilde{u_i' u_j'}}{\partial t} = \widetilde{P}_{ij} + \widetilde{T}_{ij} + \widetilde{D}_{ij} + \widetilde{\Pi}_{ij} + \widetilde{\varepsilon}_{ij}, \tag{30}$$

in which, $\widetilde{P}_{ij}$ is the phase-averaged production term; $\widetilde{T}_{ij}$ is the turbulent diffusion term; $\widetilde{D}_{ij}$ is the viscous diffusion term; $\widetilde{\Pi}_{ij}$ is the pressure-velocity interaction term; $\widetilde{\varepsilon}_{ij}$ is the viscous dissipation term. Their expressions are

$$\widetilde{P}_{ij} = -\widetilde{u_i' u_k'} \frac{\partial \widetilde{u}_j}{\partial x_k} - \widetilde{u_j' u_k'} \frac{\partial \widetilde{u}_i}{\partial x_k}, \quad \widetilde{T}_{ij} = -\frac{\partial \widetilde{u_i' u_j' u_k'}}{\partial x_k}, \quad \widetilde{D}_{ij} = \frac{1}{\text{Re}} \frac{\partial^2 \widetilde{u_i' u_j'}}{\partial x_k \partial x_k},$$

$$\widetilde{\Pi}_{ij} = -\widetilde{u_i' \frac{\partial p'}{\partial x_j}} - \widetilde{u_j' \frac{\partial p'}{\partial x_i}}, \quad \widetilde{\varepsilon}_{ij} = -\frac{2}{\text{Re}} \widetilde{\frac{\partial u_i'}{\partial x_k} \frac{\partial u_j'}{\partial x_k}}. \tag{31}$$

Figures 20(a) and 20(b) show the phase-averaged variations of the $\widetilde{u'u'}$ budget of the "*Osci*" case and the "*Coup*" case, respectively. Similarly, Figs. 20(c) and 20(d) show the phase-averaged variations of the $\widetilde{w'w'}$ budget. Comparing the "*Coup*" case with the "*Osci*" case, an overall impression is that $\widetilde{w'w'}$ decreases more dramatically than $\widetilde{u'u'}$, indicating that the source of the spanwise Reynolds stress under the coupled boundary condition is suppressed to a greater extent. This is because the wall slip significantly suppresses the viscous related diffusion process, and then prevents the energy transfer from $\widetilde{u'u'}$ to $\widetilde{w'w'}$. Compared with other terms, the fluctuation of the production term is larger, which is the main source of the fluctuation of the Reynolds normal stress. For $\widetilde{u'u'}$ at different phases of the "*Coup*" case, the peak position of $\widetilde{P}_{ij}$ is lifted to a certain extent compared with the "*Osci*" case, which is consistent with Fig. 19. For $\widetilde{w'w'}$, at most phases, the contribution of the pressure-velocity interaction exceeds the production term and becomes the
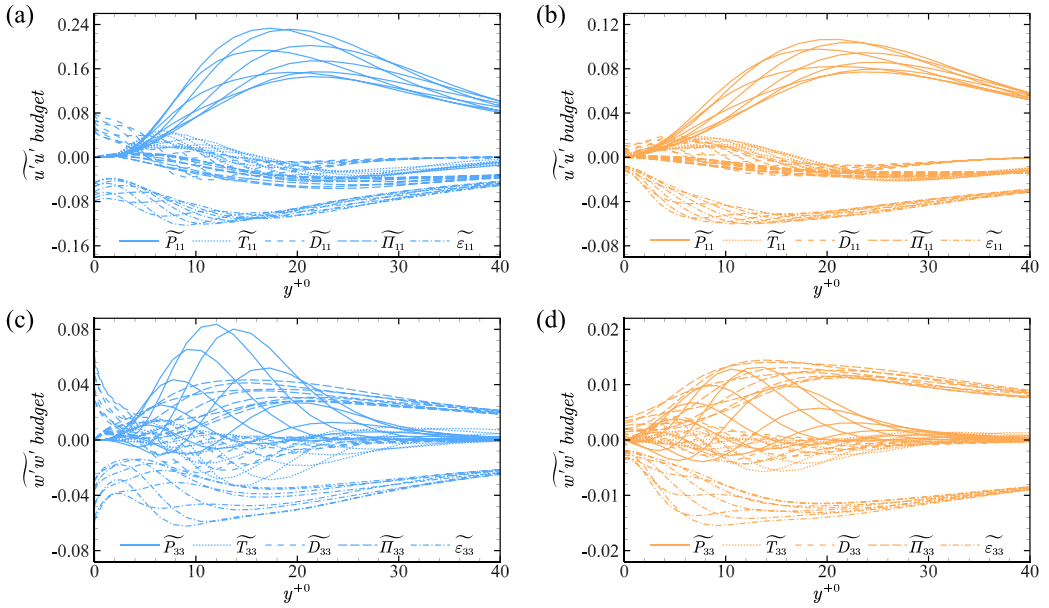
FIG. 20. Budgets of the phase-averaged [(a) and (b)] $\widetilde{u'u'}$ and [(c) and (d)] $\widetilde{w'w'}$, normalized by the inner scale of the turbulent baseline flow. The left-hand and the right-hand columns represent the results of the "*Osci*" case and the "*Coup*" case, respectively.

primary source. For both $\widetilde{u'u'}$ and $\widetilde{w'w'}$, there is no significant change in the peak position of the viscous dissipation, which can also be seen from the variation of the enstrophy, as shown in Fig. 21.

The dissipation of TKE is closely related to the enstrophy [45]. As we know from Fig. 18, the difference of $\widetilde{\omega'_y\omega'_y}$ between the "*Osci*" case and the "*Coup*" case is small. Since the current work focuses on the new changes brought by the coupling of spanwise oscillation and wall slip, only $\widetilde{\omega'_x\omega'_x}$ and $\widetilde{\omega'_z\omega'_z}$ are concerned in the current work. Figures 21(a) and 21(b) show the contours of the phase-averaged $\widetilde{\omega'_x\omega'_x}$ and $\widetilde{\omega'_z\omega'_z}$, respectively. For both the "*Osci*" and the "*Coup*" cases, the two enstrophy components at the near-wall region are changing in step with the periodic fluctuations of the friction coefficients. When the enstrophy components increase with the phase, the friction coefficients rise,
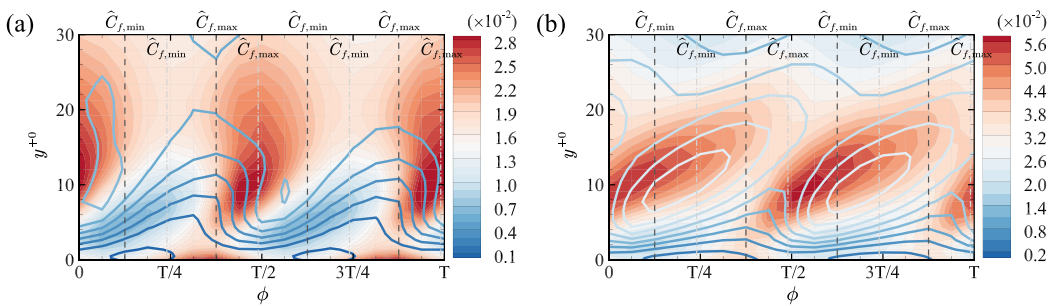

FIG. 21. Contours of the phase-averaged (a) $\widetilde{\omega'_x\omega'_x}$ and (b) $\widetilde{\omega'_z\omega'_z}$, normalized by the inner scale of the turbulent baseline flow. The contour maps represent the results of the "*Osci*" case, and the colored contour lines represent the results of the "*Coup*" case, using the same color legend. The vertical dashed lines have the same meaning as in Fig. 17.

and when the enstrophy components decrease with the phase, the friction coefficients also decrease. Hence, the lag phase of the enstrophy is the same as the phase-averaged friction coefficient. These results indicate that the enstrophy is closely correlated with the evolution of the skin-friction drag. In addition, the peak positions of the enstrophy components do not have obvious elevation like Reynolds stress.

The budget of the phase-averaged enstrophy can be written as

$$\frac{\partial}{\partial t}\left(\frac{1}{2}\widetilde{\omega'_i \omega'_i}\right) = \widetilde{P_\omega} + \widetilde{S_\omega} + \widetilde{T_\omega} + \widetilde{D_\omega} + \widetilde{\varepsilon_\omega}, \tag{32}$$

where $\widetilde{P_\omega} = -\widetilde{u'_j \omega'_i} \partial \widetilde{\omega}_i / \partial x_j$ is the phase-averaged exchange term. $\widetilde{T_\omega}$, $\widetilde{D_\omega}$, and $\widetilde{\varepsilon_\omega}$ are the turbulent diffusion term, the viscous diffusion term, and the viscous dissipation term, respectively, which are expressed as

$$\widetilde{T_\omega} = -\frac{\partial}{\partial x_j} \widetilde{u'_j \left(\frac{1}{2}\omega'_i \omega'_i\right)}, \quad \widetilde{D_\omega} = \nu \frac{\partial^2}{\partial x_j \partial x_j} \widetilde{\frac{1}{2}\omega'_i \omega'_i}, \quad \widetilde{\varepsilon_\omega} = -\nu \widetilde{\frac{\partial \omega'_i}{\partial x_j} \frac{\partial \omega'_i}{\partial x_j}}. \tag{33}$$

The vortex stretching term $\widetilde{S_\omega} = \widetilde{S^1_\omega} + \widetilde{S^2_\omega} + \widetilde{S^3_\omega}$, in which $\widetilde{S^1_\omega} = \widetilde{\omega'_i \omega'_j} \widetilde{s}_{ij}$, $\widetilde{S^2_\omega} = \widetilde{\omega}_j \widetilde{\omega'_i s'_{ij}}$, and $\widetilde{S^3_\omega} = \widetilde{\omega'_i \omega'_j s'_{ij}}$. $s_{ij} = (\partial u_i / \partial x_j + \partial u_j / \partial x_i)/2$ is the strain rate tensor. Both the average deformation $\widetilde{s}_{ij}$ and the fluctuating deformation s'_{ij} contribute to the process of vortex stretching. For the phase-averaged $\widetilde{\omega'_x \omega'_x}$ and $\widetilde{\omega'_z \omega'_z}$, their budgets can be written as

$$\frac{\partial}{\partial t}\left(\frac{1}{2}\widetilde{\omega'_x \omega'_x}\right) = \widetilde{P^x_\omega} + \widetilde{S^x_\omega} + \widetilde{T^x_\omega} + \widetilde{D^x_\omega} + \widetilde{\varepsilon^x_\omega}, \quad \frac{\partial}{\partial t}\left(\frac{1}{2}\widetilde{\omega'_z \omega'_z}\right) = \widetilde{P^z_\omega} + \widetilde{S^z_\omega} + \widetilde{T^z_\omega} + \widetilde{D^z_\omega} + \widetilde{\varepsilon^z_\omega}, \tag{34}$$

where $\widetilde{S^x_\omega} = \widetilde{S^{1,x}_\omega} + \widetilde{S^{2,x}_\omega} + \widetilde{S^{3,x}_\omega}$, $\widetilde{S^z_\omega} = \widetilde{S^{1,z}_\omega} + \widetilde{S^{2,z}_\omega} + \widetilde{S^{3,z}_\omega}$. The superscript x or z represents the x or z component of the corresponding term.

Figures 22(a) and 22(b) show the phase variations of the $\widetilde{\omega'_x \omega'_x}$ budget of the "*Osci*" case and the "*Coup*" case, respectively. Similarly, Figs. 22(c) and 22(d) show the phase variations of the $\widetilde{\omega'_z \omega'_z}$ budget. Comparing the "*Coup*" case with the "*Osci*" case, an overall impression is that $\widetilde{\omega'_x \omega'_x}$ decreases more than $\widetilde{\omega'_z \omega'_z}$. This is because the wall slip significantly weakens the energy transfer from $\widetilde{\omega'_z \omega'_z}$ to $\widetilde{\omega'_x \omega'_x}$. In the region outside the viscous sublayer, the productions of enstrophy are substantially balanced with the viscous dissipation. The production here includes the exchange term and the vortex stretching term. Similarly to Reynolds stress, the fluctuation of the production is always the main source of the fluctuation of the enstrophy component. For the "*Coup*" case, the presence of wall slip increases the fluctuations of viscous diffusion and dissipation near the wall. The values of $\widetilde{D^z_\omega}$ and $\widetilde{\varepsilon^z_\omega}$ in the very near wall region even exceed the corresponding results of the "*Osci*" case, but as the distance from the wall increases, their fluctuations quickly shrink to a lower level than that of the "*Osci*" case. As can be seen from Figs. 22(e), 22(f) 22(g), and 22(h), the production of the enstrophy mainly comes from the vortex stretching process. The contributions from the exchange terms $\widetilde{P^x_\omega}$ and $\widetilde{P^z_\omega}$ are always small. Among the vortex stretching terms, the fluctuations of $S^{1,x}_\omega$, $S^{1,z}_\omega$, and $S^{2,x}_\omega$, $S^{2,z}_\omega$ are larger than that of $S^{3,x}_\omega$, $S^{3,z}_\omega$, which is because S^1_ω and S^2_ω come from the interaction between the turbulent fluctuations and the mean strain. Out of the viscous sublayer, $S^{3,x}_\omega$ and $S^{3,z}_\omega$ maintain at a relatively stable level. Compared to the "*Osci*" case, the wall-normal positions where $S^{1,z}_\omega$ and $S^{2,z}_\omega$ reach the peak at different phases are closer to the wall in the "*Coup*" case, and the overall vortex stretching process becomes weaker.

According to the statistical characteristics of turbulent channel flow, the time derivative of the phase-averaged enstrophy is zero, so does the enstrophy components. Hence, the sum of all terms on the right-hand sides of Eq. (34) should also be zero, i.e., $\sum \text{RHS} = 0$. The imbalances in the budgets presented in Fig. 22 are shown in Fig. 23. Compared to the fluctuation level of the enstrophy budget, the imbalances of the three enstrophy components under each phase are small, although the
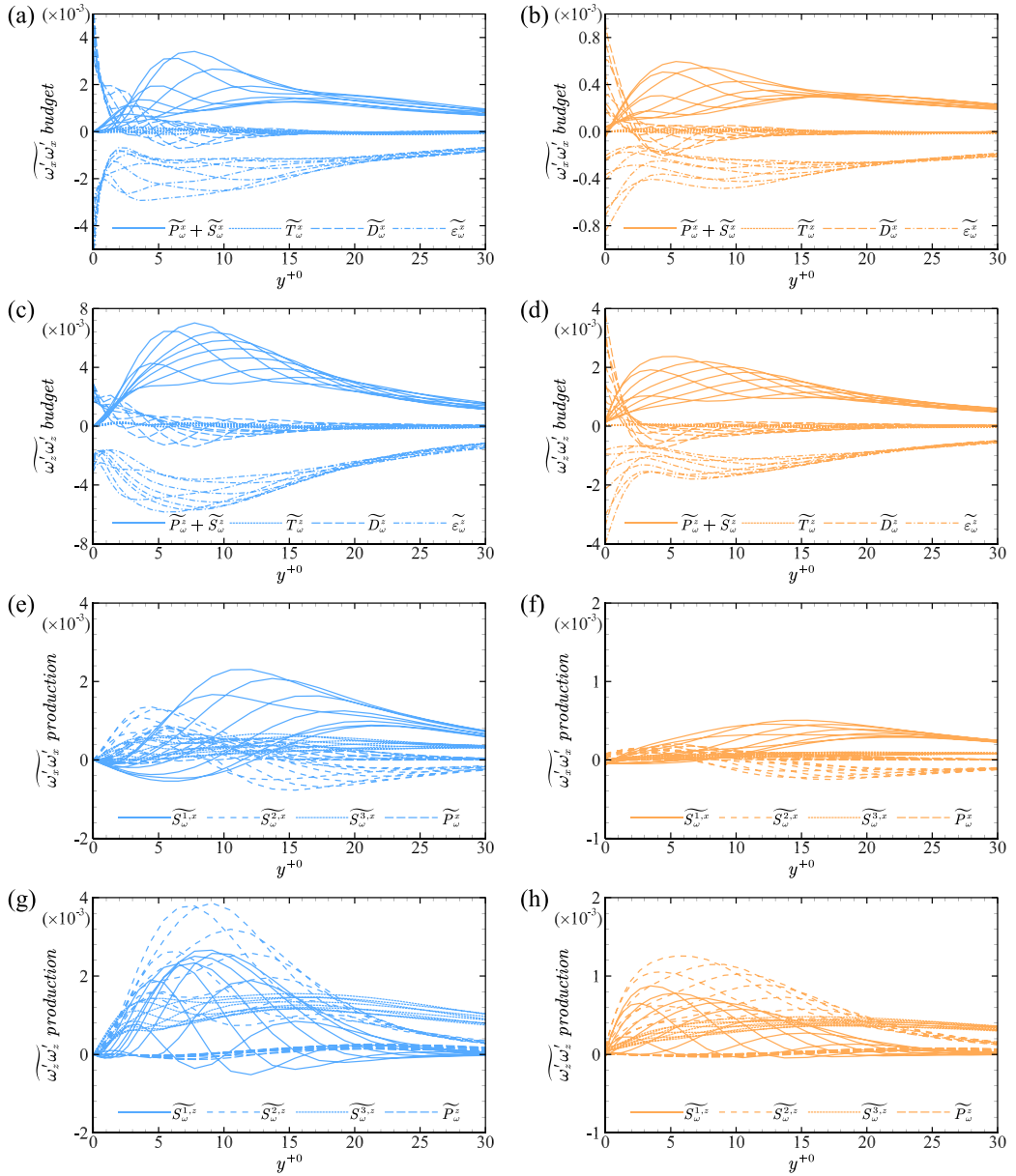
FIG. 22. Phase variations of [(a) and (b)] the $\widetilde{\omega'_x \omega'_x}$ budget and [(c) and (d)] the $\widetilde{\omega'_z \omega'_z}$ budget, as well as [(e) and (f)] the productions of $\widetilde{\omega'_x \omega'_x}$ and [(g) and (h)] the productions of $\widetilde{\omega'_z \omega'_z}$, normalized by the inner scale of the turbulent baseline flow. The left-hand and the right-hand columns represent the results of the "*Osci*" case and the "*Coup*" case, respectively.

phase-averaged results are only averaged over 20 periods. This proves that the numerical results are correct, and also reflects that the grid resolution is sufficient to distinguish the energy dissipation.

The previous analyses confirmed that the wall slip would inhibit the energy transfer process resulting from the oscillatory wall motion, including the transfer from $\widetilde{u'u'}$ to $\widetilde{w'w'}$, and the transfer from $\widetilde{\omega'_z \omega'_z}$ to $\widetilde{\omega'_x \omega'_x}$, which is to the disadvantage of the reduction of the streamwise skin-friction
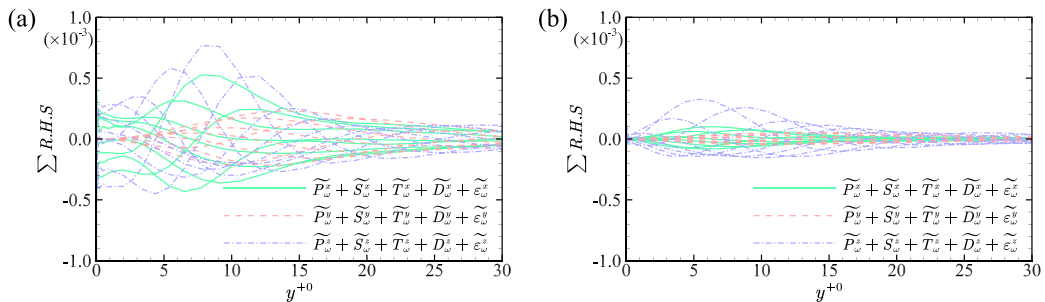
FIG. 23. Imbalances in the budgets [sum of the right-hand sides of Eq. (34)] for (a) the "*Osci*" case and (b) the "*Coup*" case. The imbalances of $\widetilde{\omega_y'\omega_y'}$ are also shown in this figure.

drag. Hence, this should also be the reason for the drag reduction loss under the coupled boundary condition. Agostini *et al.* [45] argued that the substantial fluctuations in $\widetilde{P}_{11}$ (the phase-averaged production term of $\widetilde{u'u'}$) over most of the near-wall region are reflecting the variations in the streak strength. The main mechanism of energy transfer relies on the periodical reorientation of the streak structures. Hence, the above properties indicate that the periodic inclination of the coherent structures under the coupled boundary is declining. In fact, the average elongation of the vortex tubes in the turbulent field can also be reflected by the enstrophy, and the variations in enstrophy manifest that the population of vortex structures in the flow field is significantly reduced, as shown in Sec. IV D.

D. Coherent structures

The influence of different boundary conditions on the coherent structures can be reflected by the changes of the streamwise vortices and the low-speed streaks. The vortices identified with the second invariant of the instantaneous velocity gradient tensor [50,51] (i.e., the Q criterion) are shown in Fig. 24. The background of Fig. 24 is the low-speed streaks at $y^{+0} = 5.4$. According to the DNS results, the inclination angle of streaks in different wall-normal planes is basically the same at the same instant. Compared with the turbulent baseline flow, the slip on the wall can significantly reduce the number of hairpin vortices which dominate the wall turbulence [52,53]. In contrast, under the oscillatory wall motion, the vortex structures are modulated by the periodic oscillation, and the low-speed streaks also incline cyclically. Under the coupled boundary condition, the quasi-streamwise vortices are further weakened. Moreover, in the oscillatory turbulent channel flow without slip (the "*Osci*" case), the angle between the low-speed streaks and the streamwise direction varies within the range of $\pm 29°$. For the "*Coup*" case, this range is narrowed to $\pm 16°$ (the range is calculated from the data of 16 phases in an oscillation period, and the measurement method will be introduced in the following). This is related to the decrease of the maximum spanwise velocity of the fluid on the wall under the coupled boundary condition. As the coupling effect constrains the fluctuating deformation, the population of quasi-streamwise vortices decreases dramatically, and the high skin-friction drag caused by the sweep events reduces. In addition, compared with the "*Osci*" case, the characteristic scale of the streak structures in the "*Coup*" case is larger, which can be determined by the following analysis of two-point correlation function.

In order to quantitatively investigate the periodic inclination of the streaks, the angle γ measured from the two-point correlation function of streamwise velocity fluctuations is taken as a measure for the inclination angle of the streaks. The phase-averaged two-point correlation function of streamwise velocity fluctuations can be written as

$$\widetilde{R_{u'u'}}(\Delta x, y, \Delta z) = \frac{\langle u'(x, y, z)u'(x + \Delta x, y, z + \Delta z)\rangle_{\text{phase}}}{\langle u'^2(x, y, z)\rangle_{\text{phase}}}, \tag{35}$$
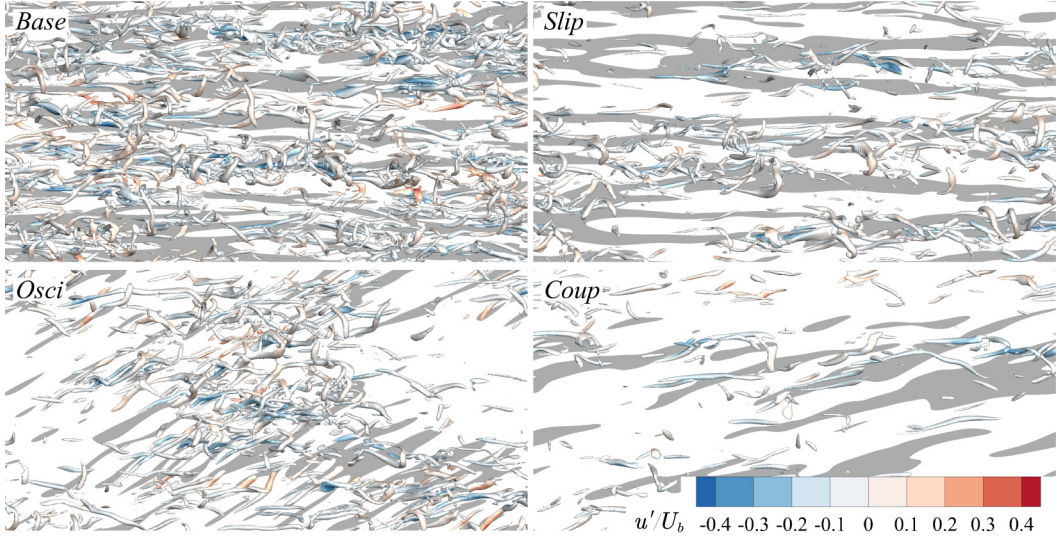
FIG. 24. Vortices identified by the Q criterion. $Q = 1$, normalized by the outer scale of the turbulent baseline flow, i.e., U_b^2/h^2. The color on the vortices represents the value of u'/U_b, i.e., the streamwise velocity fluctuations scaled with the bulk mean velocity. The background is u'/U_b at $y^{+0} = 5.4$, and the regions where $u'/U_b < -0.05$ are colored by dark grey (the low-speed streaks). The "*Osci*" case and the "*Coup*" case are in their respective phase of maximum inclination angle.

where $\langle \bullet \rangle_{\text{phase}}$ also represents the phase average. As can be seen from Figs. 25(a) and 25(b), the feature angles of the isolines with different correlation values are basically parallel, which indicates that it is of better robustness to take the feature angle of the isoline of the correlation function as a measure for the inclination angle of the streaks. In the current work, the angle between the tangent
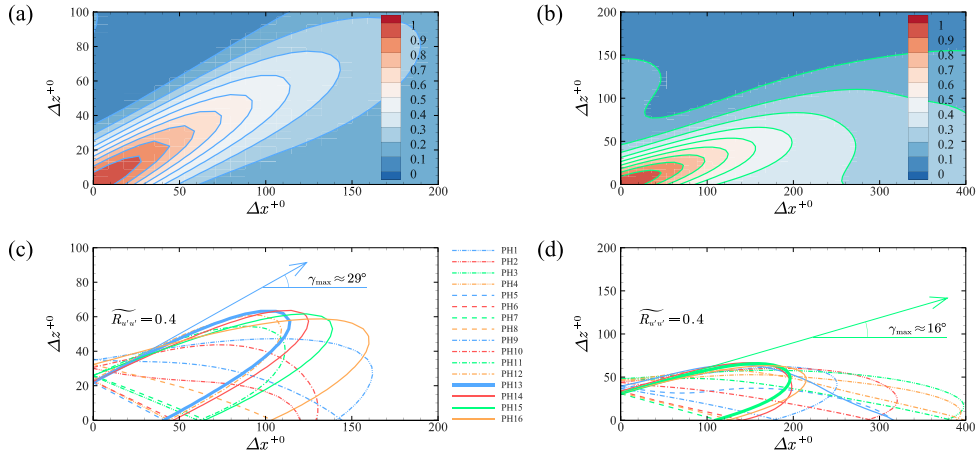

FIG. 25. Panels (a) and (b) are the contours of $\widetilde{R_{u'u'}}$ at $y^{+0} = 5.4$ of the "*Osci*" case and the "*Coup*" case, respectively. For panels (a) and (b), both cases are in their respective phase of maximum inclination angle. Panels (c) and (d) are the phase variations of the isoline with $\widetilde{R_{u'u'}} = 0.4$, including the maximum inclination angle $\gamma_{\max}$ measured from the angle between the tangent line and the streamwise direction. Panels (c) and (d) are the results of the "*Osci*" case and the "*Coup*" case, respectively. "PH1" and "PH16" stand for phase $\pi/8$ and 2π, respectively. The interval between adjacent phases is $\pi/8$.
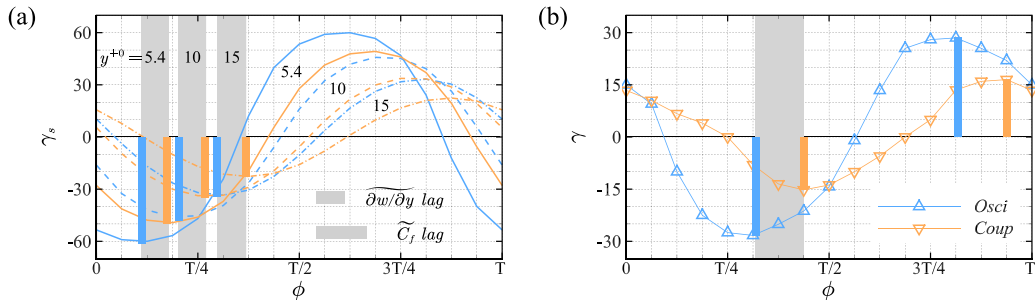
FIG. 26. (a) The phase variations of the shear angle γ_s at the $y^{+0} = 5.4$, 10, and 15 wall-normal planes and (b) the periodic change of the inclination angle γ at the $y^{+0} = 5.4$ plane. In (a), the blue and yellow lines represent the results of the "*Osci*" case and the "*Coup*" case, respectively. The solid, dashed, and dash-dot lines represent the results of the $y^{+0} = 5.4$, 10, and 15 planes, respectively. The lag phases of $\widetilde{\partial w/\partial y}$ and $\widetilde{C_f}$ are also indicated in the legend for comparison (the width of the gray rectangle). In both figures, the horizontal axis coordinates of the blue and yellow bars represent the phases corresponding to the maximum or minimum shear angles. The width of the gray area between the blue and yellow bars at the same wall-normal plane represents the lag phase.

line of $\widetilde{R_{u'u'}} = 0.4$ at $\Delta x^{+0} = 0$ and the streamwise direction is used as the inclination angle γ, as shown in Figs. 25(c) and 25(d). Additionally, the streamwise and spanwise correlation length scales under the coupled boundary condition increase obviously.

Figures 26(a) and 26(b) show the phase variations of the shear angle γ_s at the $y^{+0} = 5.4$, 10, 15 planes and the periodic change of the inclination angle γ at the $y^{+0} = 5.4$ plane, respectively. The phase-averaged shear angle γ_s is defined as $\gamma_s = \arctan (\partial \widetilde{w}/\partial y)/(\partial \widetilde{u}/\partial y)$. The phase corresponding to the maximum angle is determined by Fourier fitting of the curves. It can be found that, when the isotropic slip is applied to the oscillatory turbulent flow, the spanwise velocity, the Stokes strain, and the shear angle have the same lag phase. However, the lag phase of the inclination angle of the streaks is equivalent to the lag of the phase-averaged friction coefficient, which is larger than the Stokes strain. The coupled boundary condition has a strong inhibition on the turbulent fluctuations of the second quadrant, which raises the peak position of the Reynolds stress, and affects the process of energy transfer in the horizontal direction. As reflected in phase, the evolution of the Reynolds stress, the enstrophy and the coherent structures have greater lag than that of the Stokes strain. Because the evolution of the skin-friction drag is highly correlated with the enstrophy, the periodic fluctuation of the phase-averaged friction coefficient has the same lag phase as the turbulent energy and structures.

V. CONCLUSIONS

The coupling effect of isotropic wall slip and spanwise oscillatory wall motion is studied by DNS, which refers to the effect on the drag reduction and the turbulent dynamics. When these two boundary conditions work together on the near-wall turbulence, in addition to the respective influences on the turbulent dynamics, they also interact with each other, presenting novel statistical properties.

When the slip length is small, the drag reduction is dominated by the spanwise oscillation. The optimal oscillation period is basically the same as the value under the no-slip boundary condition, and the drag reduction is positively correlated with the wall-velocity amplitude. As the slip length increases, the contribution of the oscillatory wall motion to the drag reduction becomes weaker, and the influences of the oscillation amplitude and period gradually fade away. On the one hand, under the same slip length and oscillation period, the drag reduction loss

corresponding to the small wall-velocity amplitude is larger than that of the high wall-velocity amplitude. On the other hand, under the same slip length and wall-velocity amplitude, the drag reduction loss is basically independent of the oscillation period. The increase of slip length results in the decrease of the maximum spanwise velocity of the fluid on the wall, which reflects the coupling phenomenon and decreases the drag reduction ability of the oscillatory wall motion. Through the theoretical solution of the Stokes's second problem under the coupled boundary condition, the velocity amplitude reduction and phase lag caused by the wall slip can be well explained.

The drag reduction decomposition is conducted to describe the contributions arising from different sources. Coefficient ζ is defined to describe the drag reduction versus the outer scale slip length l_b^*. Compared with the respective no-slip reference flow, the ζ of laminar (including the laminar Couette flow and the laminar Poiseuille flow) and turbulent channel flows (including the turbulent baseline flow and the oscillatory turbulent flow) can be written in a unified form, i.e., $1/[1 + C(l_b^*)l_b^*]$. For laminar flow, C is a constant. For turbulent flow, C consists of C_1 and C_2, resulting from the effective slip on the wall and the modifications to the turbulent dynamics, respectively. As the slip length increases, C_1 remains consistent with the value of the no-slip reference flow, while the contribution represented by C_2 will undergo a shift from drag increase to drag reduction. Additionally, compared with the turbulent flow without oscillation, the critical slip length at which the contribution of C_2 changes from drag increase to drag reduction increases in the coupling case.

Furthermore, many aspects of the turbulence properties are influenced by the coupling effect. First, the coupled boundary condition mixes the effects of the wall slip and the oscillatory wall motion on the mean velocity profiles, i.e., the mean streamwise velocity in the near-wall region increases and the viscous sublayer thickens. Second, an unexpected property of the coupled boundary condition is found that the existence of the Stokes layer makes the Reynolds shear stress decrease slowly as the slip length increases, which eventually delays the relaminarization process caused by the large slip length. Third, the slip on the wall can condense the envelope range of the phase fluctuations caused by the oscillatory wall motion, as well as the magnitude of the periodic fluctuation of the phase-averaged friction coefficient. Fourth, according to the quadrant analysis, the wall slip can enhance the oscillatory wall motion to suppress the ejection events and increase the normal range where the sweep events dominate the production of the TKE. Meanwhile, the joint PDF reflects that the cross-correlation between u' and v' fluctuations is reduced. Fifth, due to the strong inhibition of the ejection events by the coupled boundary condition, the peak positions of the phase-averaged Reynolds stress $\widetilde{u'u'}$ and $\widetilde{w'w'}$ are elevated. Consistent with the variation of the phase-averaged enstrophy components $\widetilde{\omega_x'\omega_x'}$ and $\widetilde{\omega_z'\omega_z'}$, there is no significant change in the peak position of the viscous dissipation of the Reynolds normal stress. Sixth, the wall slip would narrow the periodic inclination of the streaks and then inhibit the energy transfer process resulting from the periodical reorientation of the streaks, including the transfer from $\widetilde{u'u'}$ to $\widetilde{w'w'}$, and the transfer from $\widetilde{\omega_z'\omega_z'}$ to $\widetilde{\omega_x'\omega_x'}$. Seventh, in terms of phase, a noteworthy phenomenon is that the Stokes strain and the shear angle of different wall-normal planes have the same lag phase with the spanwise velocity, while the hysteresis of turbulent dynamics leads to the larger lag phase of the streaks and phase-averaged friction coefficient.

[1] J. Lumley and P. Blossey, Control of turbulence, Annu. Rev. Fluid Mech. **30**, 311 (1998).

[2] V. Spandan, R. Verzicco, and D. Lohse, Physical mechanisms governing drag reduction in turbulent Taylor-Couette flow with finite-size deformable bubbles, J. Fluid Mech. **849**, R3 (2018).

[3] C.-H. Choi and C.-J. Kim, Large Slip of Aqueous Liquid Flow Over a Nanoengineered Superhydrophobic Surface, Phys. Rev. Lett. **96**, 066001 (2006).

[4] J. P. Rothstein, Slip on superhydrophobic surfaces, Annu. Rev. Fluid Mech. **42**, 89 (2010).

[5] P. Lv, Y. Xue, Y. Shi, H. Lin, and H. Duan, Metastable States and Wetting Transition of Submerged Superhydrophobic Structures, Phys. Rev. Lett. **112**, 196101 (2014).

[6] Y. Xue, P. Lv, H. Lin, and H. Duan, Underwater superhydrophobicity: Stability, design and regulation, and applications, Appl. Mech. Rev. **68**, 030803 (2016).

[7] Y. Xiang, S. Huang, P. Lv, Y. Xue, Q. Su, and H. Duan, Ultimate Stable Underwater Superhydrophobic State, Phys. Rev. Lett. **119**, 134501 (2017).

[8] C. Lee, C.-H. Choi, and C.-J. Kim, Superhydrophobic drag reduction in laminar flows: A critical review, Exp. Fluids **57**, 176 (2016).

[9] J. Ou, B. Perot, and J. P. Rothstein, Laminar drag reduction in microchannels using ultrahydrophobic surfaces, Phys. Fluids **16**, 4635 (2004).

[10] C. Lee, C.-H. Choi, and C.-J. Kim, Structured Surfaces for a Giant Liquid Slip, Phys. Rev. Lett. **101**, 064501 (2008).

[11] A. Busse, N. D. Sandham, G. McHale, and M. I. Newton, Change in drag, apparent slip and optimum air layer thickness for laminar flow over an idealized superhydrophobic surface, J. Fluid Mech. **727**, 488 (2013).

[12] Y. Li, K. Alame, and K. Mahesh, Feature-resolved computational and analytical study of laminar drag reduction by superhydrophobic surfaces, Phys. Rev. Fluids **2**, 054002 (2017).

[13] C. C. Mei and X. Y. Guo, Numerical study of laminar boundary-layer flows over a superhydrophobic plate, Phys. Fluids **30**, 072002 (2018).

[14] A. T. Tran, H. L. Quang, and Q.-C. He, Effective interfacial conditions for the Stokes flow of a fluid on periodically rough surfaces, Acta Mech. **228**, 1851 (2017).

[15] S. K. Aghdam and P. Ricco, Laminar and turbulent flows over hydrophobic surfaces with shear dependent slip length, Phys. Fluids **28**, 035109 (2016).

[16] K. Fukagata, N. Kasagi, and P. Koumoutsakos, A theoretical prediction of friction drag reduction in turbulent flow by superhydrophobic surfaces, Phys. Fluids **18**, 051703 (2006).

[17] G. A. Zampogna, J. Magnaudet, and A. Bottaro, Generalized slip condition over rough surfaces, J. Fluid Mech. **858**, 407 (2019).

[18] R. J. Daniello, N. E. Waterhouse, and J. P. Rothstein, Drag reduction in turbulent flows over superhydrophobic surfaces, Phys. Fluids **21**, 085103 (2009).

[19] H. Park, G. Sun, and C.-J. Kim, Superhydrophobic turbulent drag reduction as a function of surface grating parameters, J. Fluid Mech. **747**, 722 (2014).

[20] J. Zhang, H. Tian, Z. Yao, P. Hao, and N. Jiang, Mechanisms of drag reduction of superhydrophobic surfaces in a turbulent boundary layer flow, Exp. Fluids **56**, 179 (2015).

[21] J. W. Gose, K. Golovin, M. Boban, J. M. Mabry, A. Tuteja, M. Perlin, and S. L. Ceccio, Characterization of superhydrophobic surfaces for drag reduction in turbulent flow, J. Fluid Mech. **845**, 560 (2018).

[22] S. Grossmann, D. Lohse, and C. Sun, High-Reynolds number Taylor-Couette turbulence, Annu. Rev. Fluid Mech. **48**, 53 (2016).

[23] T. Min and J. Kim, Effects of hydrophobic surface on skin friction drag, Phys. Fluids **16**, L55 (2004).

[24] M. B. Martell, J. B. Perot, and J. P. Rothstein, Direct numerical simulations of turbulent flows over superhydrophobic surfaces, J. Fluid Mech. **620**, 31 (2009).

[25] A. Busse and N. D. Sandham, Influence of an anisotropic slip-length boundary condition on turbulent channel flow, Phys. Fluids **24**, 055111 (2012).

[26] A. Rastegari and R. Akhavan, On the mechanism of turbulent drag reduction with superhydrophobic surfaces, J. Fluid Mech. **773**, R4 (2015).

[27] G. Gómez-de-Segura, C. T. Fairhall, M. MacDonald, D. Chung, and R. García-Mayoral, Manipulation of near-wall turbulence by surface slip and permeability, J. Phys.: Conf. Ser. **1001**, 012011 (2018).

[28] L. Guo, S. Chen, and M. O. Robbins, Effective slip boundary conditions for sinusoidally corrugated surfaces, Phys. Rev. Fluids **1**, 074102 (2016).

[29] T. Jung, H. Choi, and J. Kim, Effects of the air layer of an idealized superhydrophobic surface on the slip length and skin-friction drag, J. Fluid Mech. **790**, R1 (2016).

[30] J. Seo, R. García-Mayoral, and A. Mani, Turbulent flows over superhydrophobic surfaces: Flow-induced capillary waves, and robustness of air-water interfaces, J. Fluid Mech. **835**, 45 (2018).

[31] J. Seo and A. Mani, Effect of texture randomization on the slip and interfacial robustness in turbulent flows over superhydrophobic surfaces, Phys. Rev. Fluids **3**, 044601 (2018).

[32] H. Park, H. Park, and J. Kim, A numerical study of the effects of superhydrophobic surface on skin-friction drag in turbulent channel flow, Phys. Fluids **25**, 110815 (2013).

[33] A. Rastegari and R. Akhavan, The common mechanism of turbulent skin-friction drag reduction with superhydrophobic longitudinal microgrooves and riblets, J. Fluid Mech. **838**, 68 (2018).

[34] J. Seo and A. Mani, On the scaling of the slip velocity in turbulent flows over superhydrophobic surfaces, Phys. Fluids **28**, 025110 (2016).

[35] G. E. Karniadakis and K.-S. Choi, Mechanisms on transverse motions in turbulent wall flows, Annu. Rev. Fluid Mech. **35**, 45 (2003).

[36] M. Quadrio, Drag reduction in turbulent boundary layers by in-plane wall motion, Phil. Trans. R. Soc. A **369**, 1428 (2011).

[37] M. Zhao, W. Huang, and C. Xu, Drag reduction in turbulent flows along a cylinder by streamwise-travelling waves of circumferential wall velocity, J. Fluid Mech. **862**, 75 (2019).

[38] W. J. Jung, N. Mangiavacchi, and R. Akhavan, Suppression of turbulence in wall-bounded flows by high-frequency spanwise oscillations, Phys. Fluids A **4**, 1605 (1992).

[39] K.-S. Choi, Near-wall structure of turbulent boundary layer with spanwise-wall oscillation, Phys. Fluids **14**, 2530 (2002).

[40] P. Ricco, Modification of near-wall turbulence due to spanwise wall oscillations, J. Turbul. **5**, N24 (2004).

[41] J.-I. Choi, C. Xu, and H. J. Sung, Drag reduction by spanwise wall oscillation in wall-bounded turbulent flows, AIAA J. **40**, 842 (2002).

[42] M. Quadrio and P. Ricco, Critical assessment of turbulent drag reduction through spanwise wall oscillations, J. Fluid Mech. **521**, 251 (2004).

[43] E. Touber and M. A. Leschziner, Near-wall streak modification by spanwise oscillatory wall motion and drag reduction mechanisms, J. Fluid Mech. **693**, 150 (2012).

[44] S. Lardeau and M. A. Leschziner, The streamwise drag reduction response of a boundary layer subjected to a sudden imposition of transverse oscillatory wall motion, Phys. Fluids **25**, 075109 (2013).

[45] L. Agostini, E. Touber, and M. A. Leschziner, Spanwise oscillatory wall motion in channel flow: Drag reduction mechanisms inferred from DNS-predicted phase-wise property variations at $\text{Re}_\tau = 1000$, J. Fluid Mech. **743**, 606 (2014).

[46] G. E. Karniadakis, M. Israeli, and S. A. Orszag, High-order splitting methods for the incompressible Navier-Stokes equations, J. Comput. Phys. **97**, 414 (1991).

[47] J. Kim, P. Moin, and R. Moser, Turbulence statistics in fully developed channel flow at low Reynolds number, J. Fluid Mech. **177**, 133 (1987).

[48] O. Iida and Y. Nagano, The relaminarization mechanisms of turbulent channel flow at low Reynolds numbers, Flow, Turbul. Combus. **60**, 193 (1998).

[49] N. E. Huang, Z. Shen, S. R. Long, M. C. Wu, H. H. Shih, Q. Zheng, N.-C. Yen, C. C. Tung, and H. H. Liu, The empirical mode decomposition and the Hilbert spectrum for nonlinear and non-stationary time series analysis, Proc. R. Soc. Lond. A **454**, 903 (1998).

[50] J. Jeong and F. Hussain, On the identification of a vortex, J. Fluid Mech. **285**, 69 (1995).

[51] Z. Li, B. Hu, S. Lan, J. Zhang, and J. Huang, Control of turbulent channel flow using a plasma-based body force, Comput. Fluids **119**, 26 (2015).

[52] C. Xu, B. Deng, W. Huang, and G. Cui, Coherent structures in wall turbulence and mechanism for drag reduction control, Sci. China Phys. Mech. Astron. **56**, 1053 (2013).

[53] S. K. Robinson, Coherent motions in the turbulent boundary layer, Annu. Rev. Fluid Mech. **23**, 601 (1991).